Pharmaco-genomic investigations of organo-iridium anticancer complexes reveal novel mechanism of action

For submission to Metallomics

Pharmaco-genomic investigations of organo-iridium anticancer complexes reveal novel mechanism of action†

Jessica M Hearn* [1,2], George M. Hughes* [1,3], Isolda Romero-Canelón[1,4], Alison F. Munro[5], Belén Rubio-Ruiz[5], Zhe Liu[1,6], Neil O. Carragher[5], and Peter J. Sadler[1]

[1]Department of Chemistry, University of Warwick, UK.

[2]Warwick Systems Biology Centre, University of Warwick, UK.

[3]MOAC DTC, University of Warwick, UK.

[4]School of Pharmacy, University of Birmingham, UK.

[5]Cancer Research UK Edinburgh Centre, Institute of Genetics and Molecular Medicine, University of Edinburgh, UK.

[6] Department of Chemistry and Chemical Engineering, Qufu Normal University, China.

* These two authors contributed equally to this work

E-mail: p.j.sadler@warwick.ac.uk;
Fax: +44 (0)24 7652 3819; Tel: +44 (0)24 7652 3818

†Electronic supplementary information (ESI) available. See DOI: xxxxx

Abstract

Resistance to platinum drugs (used in >50% of cancer chemotherapies) is a clinical problem. Other precious metal complexes with distinct mechanisms of action might overcome this. Half-sandwich organometallic complexes containing arene or cyclopentadienyl (Cp) ligands show promise. We screened two iridium(III) complexes $[Ir(Cp^{xbiph})(ppy)Cl]$ (ZL49, **1**, ppy=phenylpyridine) and $[Ir(Cp^{xph})(azpyNMe_2)Cl]PF_6$ (ZL109, **2**, $azpyNMe_2$=N,N-dimethylphenylazopyridine) in 916 cancer cell lines from 28 tissue types. On average, complex **2** was 78x more potent than **1**, 36x more active than cisplatin (CDDP), and strongly active (nanomolar) in patient-derived ovarian cancer cell lines. RNA sequencing of A2780 ovarian cells revealed upregulation of antioxidant responses (NRF2, AP-1) consistent with observed induction of reactive oxygen species (ROS). Protein microarrays,

high content imaging and cell cycle analysis showed S/G2 arrest, and late-stage DNA damage response without p53 requirement. The triple-negative breast cancer cell line OCUB-M was highly sensitive to **2** as were cell lines with KIT mutations. Complex **2** exhibits a markedly different pattern of antiproliferative activity compared to the 253 drugs in the Sanger Cancer Genome database, but is most similar to osmium(II) arene complexes which share the same azopyridine ligand. Redox modulation and DNA damage can provide a multi-targeting strategy, allowing compounds such as **2** to overcome cellular resistance to platinum anticancer drugs.

Keywords:
Organo-iridium complexes, phenotypic screening, RNA sequencing, mechanism of action, Reactive Oxygen Species, apoptosis

Significance to Metallomics

Half-sandwich organoiridium complexes show promising activity, with novel mechanisms of action that may combat platinum resistance and side effects seen commonly in current anticancer chemotherapy regimes. The field of systems pharmacology provides methods to elucidate the often multitargeted mechanisms of metallodrugs. Here, we explore the link between transcriptomic and phenotypic data in ovarian cancer cells, using state-of-the-art high-throughput methods, together with data collected from Sanger's Genomics of Drug Sensitivity in Cancer screen and primary tumour cell lines. Our studies ultimately reveal not only the subtle effects of ligands on complex activity, but unique mechanisms shared only with osmium arene complexes.

.

Introduction

The square-planar platinum drugs cisplatin (CDDP), carboplatin and oxaliplatin are now used in over 50% of cancer chemotherapies, but intrinsic and acquired resistance represent major clinical problems across cancer indications. CDDP has a primary mechanism of action (MoA) which involves DNA targeting, induction of DNA bending, and apoptosis.[1] Other precious metal complexes might be able to overcome resistance if they have different MoAs. This appears to be the case for platinum drug oxaliplatin and candidate drug phenanthriplatin, which are not cross-resistant with CDDP. Although oxaliplatin is classified as a DNA alkylating agent like CDDP, recent evidence now points primarily to ribosome biogenesis stress, rather than DNA damage.[2]

Pseudo-octahedral 'half-sandwich' organometallic arene and cyclopentadienyl complexes also show promise for overcoming platinum resistance. Osmium(II) arene complexes and iridium(III) cyclopentadienyl (Cp^x) complexes $[M(arene/Cp^X)(N,N)(X)]^{n+}$ can target DNA when N,N is a chelated diamine ligand.[3,4] In contrast, when N,N is an azopyridine ligand, the complexes can cause redox stress in cancer cells and target mitochondrial metabolism.[5–8] Azopyridine ligands are strong π-acceptors and withdraw electron density from the metal making the M-C bond to the monodentate ligand X (e.g. Cl or I) much less reactive.

We have discovered potent antiproliferative activity for organo-Os(II) and organo-Ir(III) complexes by phenotypic screening and have shown that screening in the National Cancer Institute (NCI-60) and Sanger 800+ panel of cancer cell lines when combined with transcriptomics, reactive oxygen species (ROS), protein micro-arrays, high content imaging and other assays can provide valuable insight into their MoAs.[9,10]

Here we report the results of phenotypic screening and in-depth MoA profiling of two organo-iridium(III) complexes (Figure 1) [Ir(η^5-Cp^{xbiph})(ppy)Cl] (ZL49, **1**, ppy = phenylpyridine) and [Ir(η^5-Cp^{xph})(azpyNMe$_2$)Cl]PF$_6$ (ZL109, **2**, azpyNMe$_2$ = N,N-dimethylphenylazopyridine) in the Sanger Cancer Genome project panel of 916 cancer cell lines with known gene sequences from 28 tissue types. Time-dependent up- and down-regulation of genes has been studied by RNA sequencing, together with the detection of selected proteins and quantitative analysis of cell cycle, and apoptosis phenotypes.

These studies point to a unique MoA for organo-iridium complexes with little in common with previously-screened agents, except organo-osmium complexes.

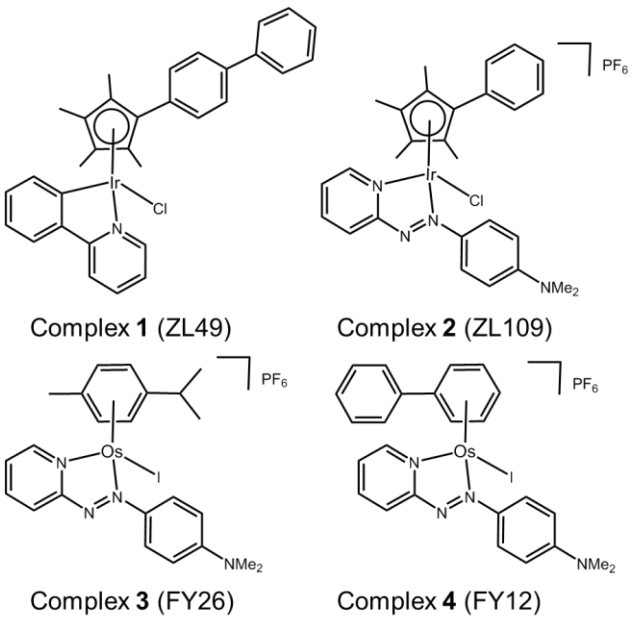

Fig. 1. Organo-Ir(III) complexes **1** and **2** and organo-Os(II) complexes **3** and **4** referenced in this work.

Results

Antiproliferative activity

Initially, we screened organo-iridium complexes **1** ([Ir(η^5-Cp^{xbiph})(ppy)Cl]) and **2** ([Ir(η^5-Cp^{xph})(azpy-NMe$_2$)Cl]PF_6 in the NCI-60 screen.[8,11] Complex **1** was more active than **2**, however both were potent with mean IC_{50} values of <1 μM, more potent than the clinical drug CDDP. Both compounds were particularly active in colorectal cell line COLO205 and breast cell line MDA-MB-468, with renal cell lines showing resistance (much lower sensitivity) to both.

The higher activity of complexes **1** and **2** towards COLO205 and MDA-MB-468 can be attributed to redox deficiencies in these cell lines. COLO205 colorectal cells have reduced levels of glutathione-S-transferase P1 (GSTP1), an enzyme which detoxifies drugs by conjugating them to glutathione (GSH) often limiting the efficacy of anticancer agents.[12] Without this enzyme, there may be less conjugation and inactivation by GSH, which could increase the sensitivity of cells towards anticancer compounds.

The breast cell line, MDA-MB-468 showed a consistently high sensitivity in the NCI-60 screen(IC_{50} values 17 nM to 1.8 μM). This cell line has a glucose 6-phosphate dehydrogenase (G6PD) A phenotype, meaning it lacks the proper functioning of this enzyme in the pentose phosphate pathway.[13] G6PD is the rate-limiting enzyme in this pathway; its deficiency blocks the conversion of glucose-6-phosphate to 6-phosphoglucono-d-lactone and in the process prevents the conversion of NADPH to $NADP^+$, a required step in GSH synthesis.[14] This suggests that a GSH deficiency may play an important role in potentiating the activity, something previously demonstrated when A2780 cells were co-incubated with low levels of the GSH inhibitor, L-buthionine sulfoximine. Multiple studies have shown that this deficiency prevents the cells from mediating oxidative stress, and often results in apoptosis and necrosis of cells in patients.[15]

Comparison of the patterns of selectivity for both complexes with those of >40,000 synthetic compounds and natural products in the NCI database and drugs that showed a Pearson's correlation coefficient (*r*) > 0.5, revealed only 3 drugs with similar patterns of selectivity to that of **1** and **2**, highlighting their novelty.

Now we have screened complexes **1** and **2** in 916 cell lines from 28 tissue types in the Sanger Cancer Genome project panel and compared the patterns of antiproliferative activity with the 256 compounds in the 'Genomics of Drug Sensitivity in Cancer' database.[16]

In Figure 2, the IC_{50} values for **1** and **2** and CDDP are compared for 809 cell lines in the screen using box and whisker plots. On average across all cell lines, complex **2** is 78x more potent than complex **1** and 36x more potent than CDDP.

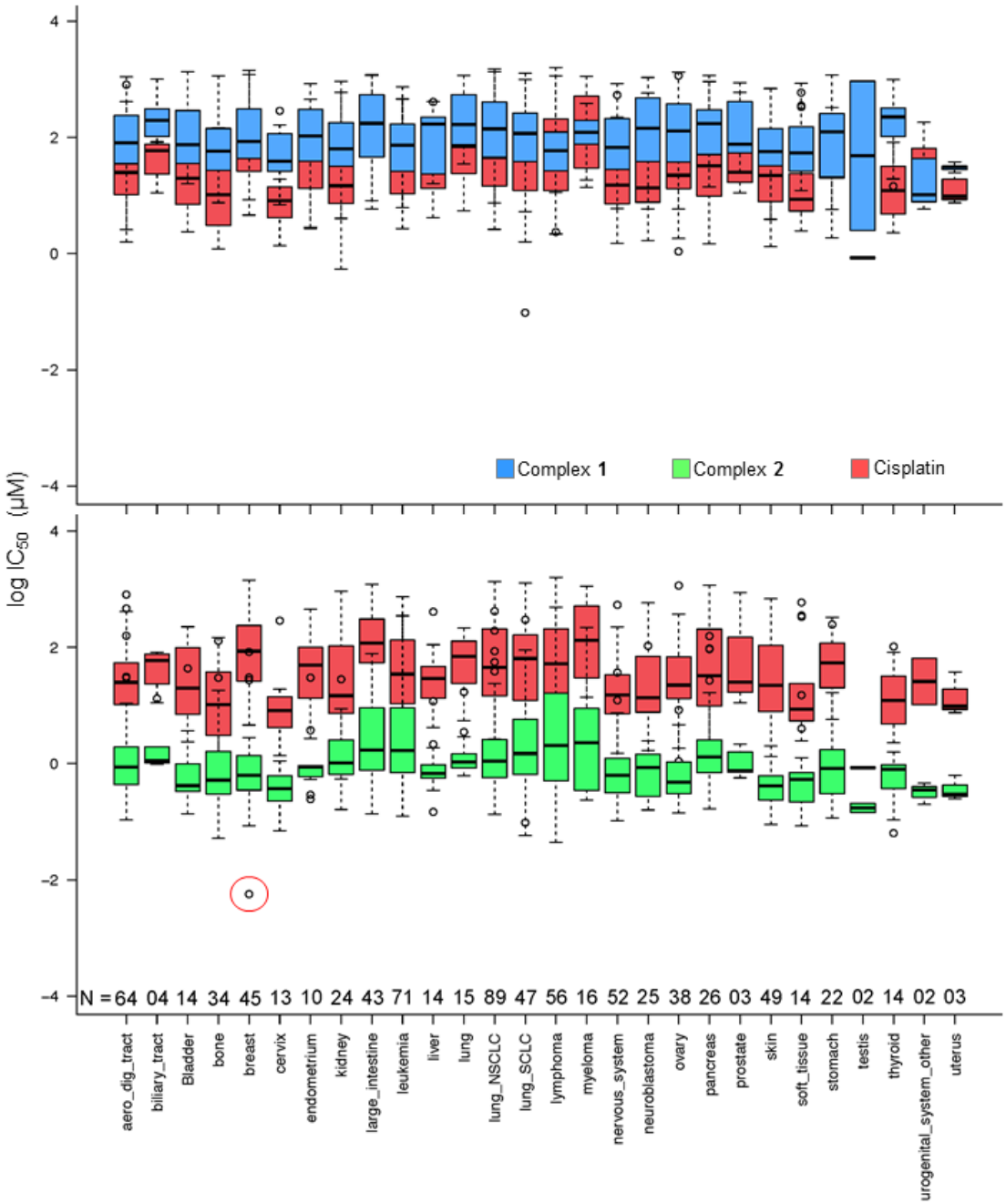

Fig. 2. Box and whisker plots for log IC_{50} (μM) values, complex **1** (blue), **2** (green) and CDDP (red) in the Sanger screen, separated by tissue type. N denotes the number of cell lines of each tissue type in the screen. The red circle denotes the IC_{50} value for the breast cancer line OCUB-M that exhibits extreme sensitivity to **2** and, in contrast, low sensitivity to both **1** and CDDP. Total number of cell lines included = 809 (To match the cell lines screened against CDDP). IC_{50} values which fall outside the experimental screening concentrations were calculated using a curve-fitting algorithm, and as such have a large confidence interval.[16]

Complex **2** exhibits its highest mean activity in cancers of testicular, urogenital, cervical and uterine tissues, although the number of cell lines derived from these tissues is considerably lower than for many of the other tissue types. Complex **1** shows its highest activity in the SU-DHL-5 lymphoma cell line; however, this potency is lower than that of **2** and CDDP.

Complex **2** displays its highest activity in the OCUB-M breast cancer cell line, and notably is ca. 5 orders of magnitude more active than CDDP. OCUB-M is a triple negative breast cancer cell line with high expression of E-cadherin and laminin receptors.[17] There are 10 genetic mutations in this cell line, one of which is a missense mutation in p53. In previous work it was also shown that MDA-MB-468, another triple negative cell line, had significant susceptibility to **2**.[8] MDA-MB-468 lacks the appropriate machinery to respond to ROS through a deficiency in glucose 6-phosphate dehydrogenase. Triple-negative breast cancer is particularly difficult to treat; therefore further studies of **2** in this area would seem warranted.

Complex **2** and the organo-osmium complex FY12 (complex **4** in Figure 1), which notably contains the same chelated azopyridine ligand, are amongst the 15 most potent drugs screened against OCUB-M in the Sanger panel. Five others are microtubule-targeting drugs, constituting all the drugs in this category in the screen. The successful treatment of OCUB-M with microtubule inhibitors may be linked to the over-expression of *TUBG1* (tubulin SF) and *MAP7* (microtubule-associated protein) and the down-regulation of *MAP1LC3B* (microtubule associated protein 1 light chain 3 beta), *MICAL-1* (microtubule associated monooxygenase, calponin and LIM domain containing 1) and *TTBK2* (Tau tubulin kinase). The over-expressed genes mediate microtubule formation and stabilisation. The down-regulated genes can cause destabilisation and depolymerisation of tubulin and actin, respectively.

Although sensitive to complex **2,** OCUB-M is highly insensitive to CDDP. This might be linked to mutations in its p53 protein, which has been repeatedly correlated with CDDP resistance.[18] Figure S1 shows the distribution of IC_{50}

values for **1**, **2** and CDDP, where boxes show the median, upper and lower quartiles. Whiskers extend to whichever is the lower value of the upper/lower quartile +1.5x the interquartile range, or the maximum/minimum y value, respectively. The red lines mark the threshold for lower sensitivity compared to complex **2**. Complex **2** shows considerably higher activity than complex **1** (by 78x) and CDDP (by 36x), as well as being significantly more potent when compared to the mean activity over all ca. 200 drugs included in the screen (Table S4). The IC_{50} values for 46 of the 916 cell lines lie above the upper whisker threshold for **2**. This population of less sensitive cell lines falls within the activity ranges of **1** and CDDP. The occurrence of so many cell lines far outside the interquartile range for **2** might be due to a common resistance feature, although may also reflect the tighter spread amongst values for the more sensitive cell lines.

Table 1 lists the 10 cell lines exhibiting the lowest sensitivity to complex **2**. The tissue types displaying the highest percentages are lymphoma, myeloma and leukemia, each with >10% of their population less sensitive to **2** (Figure S2). These particular tissues make up the blood-derived cancers. Although some factor specific to tissues derived from the embryonic mesoderm may contribute to the low sensitivity, other mesodermally-derived tissues, such as bone, urogenital and kidney tissue do not exhibit a large proportion of resistant cells, making it more likely that some other feature of blood-derived cancers confers resistance. Cancers of ectodermally-derived tissues such as the skin and nervous system show little or no cell lines in the resistant population.

Table 1. The 10 cell lines least sensitive to complex **2** (IC_{50} > 150 μM). The drug in the database associated with the lowest sensitivity for each cell line is also shown, together with the target of that drug.

Subtype	Cell line	Resistance drug	Drug Target
Lung	LU-65	Vorinostat and Piperlongumine	HDAC
	NCI-H2081	Piperlongumine	Increases ROS Levels
	NCI-H2135	Piperlongumine	Increases ROS Levels
Lymphoma	WSU-DLCL2	LAQ824	HDAC
	A4-Fuk	N/A	N/A
Aerodigestive	ESO51	Piperlongumine	Increases ROS Levels
	OACM5-1	TW 37	BCL-2, BCL-XL
Leukemia	PF-382	Piperlongumine	Increases ROS Levels
Myeloma	U-266	NU-7441	DNAPK
Stomach	NCI-SNU-1	BEZ235	PI3K, mTORC1/2

It is apparent that resistance to piperlongumine treatment is common for these cell lines: 19 out of 46 cell lines least sensitive to complex **2** can also classified as resistant to piperlongumine, an organic natural product isolated from the fruit of the pepper plant Piper longum. Piperlongumine has been evaluated as a novel senolytic agent, selectively inducing death of senescent cells,[19] killing cancer cells by targeting the stress response to ROS.[20]

The level of similarity between **1** and **2** with other drugs in the screen was evaluated from differences in their IC_{50} values. To account for the fact that large positive and large negative differences could cancel each other out, the standard deviations of these differences were also calculated. A drug was considered similar to the index drug if the total mean difference in IC_{50} was close to zero and the SD was low (denoted by the red circle in Figure 3).

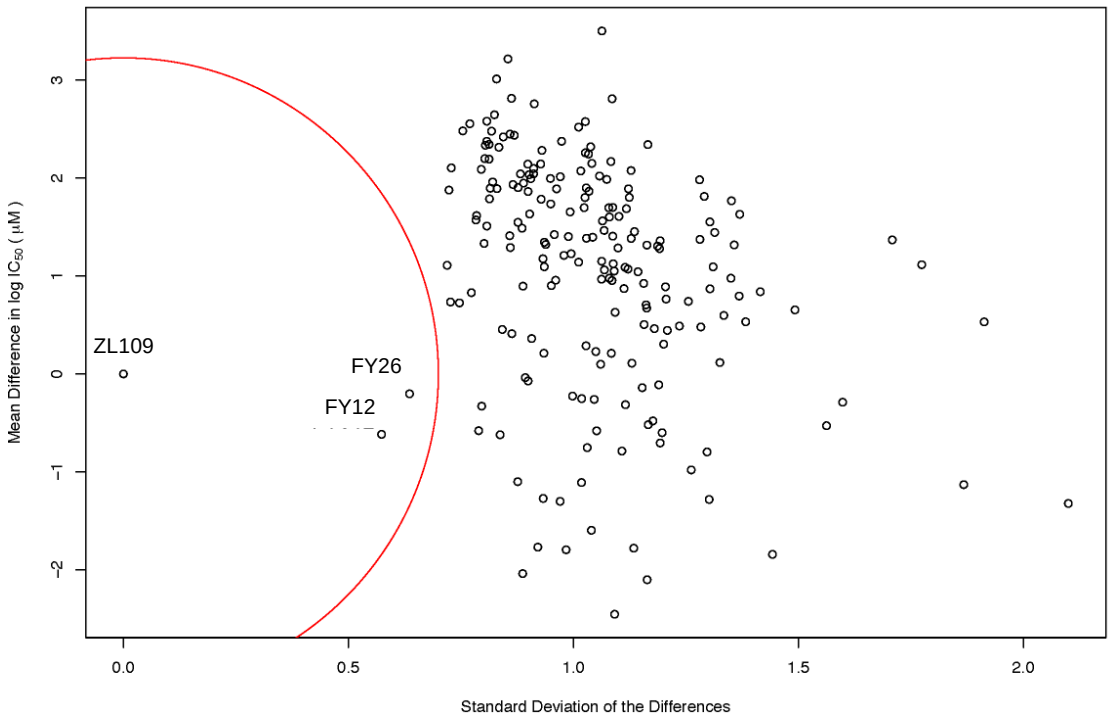

Fig. 3. Scatter plot of the mean difference in log IC_{50} values (µM) between all screened drugs and complex **2** (ZL109) vs. the SD of these differences. The red circle of radius 0.7 standard deviations denotes a 'region of significant similarity where the mean difference and standard deviation are low. The similarity with two osmium arene complexes which share the same chelated azopyridine ligand (complexes **3** (FY26) and **4** (FY12), Figure 1) is evident.

Intriguingly, the data for iridium complex **2** matched most closely those of FY12 ($[Os(\eta^6\text{-bip})(azpy\text{-}NMe_2)I]^+$) and FY26 ($[Os(\eta^6\text{-}p\text{-cym})(azpy\text{-}NMe_2)I]^+$), (complexes **4** and **3** respectively, in Figure 1) two organo-osmium compounds studied previously in our laboratory.[21] FY12/FY26 and **2** share the same bidentate azopyridine ligand, but have different C-bound π-donor ligands (neutral arene versus negatively-charged cyclopentadienyl), different monodentate halido ligands (chloride versus iodide) as well as metal centres (Os(II) versus Ir(III)). The much higher similarity of these two matches to complex **2** compared to other drugs tested in the screen is evident demonstrating novelty in the MoA of complex **2** (Figure 3).

To extract significant correlations between activity and oncogenic behaviour of compounds from the Sanger screen, an analysis of variance (ANOVA) test can be used. The dependent variable is presented as an n x 2 matrix for each

compound, containing IC_{50} and b (slope) values, and therefore, a multivariate ANOVA (MANOVA) is used for the analysis. For each gene, a linear model explains these activity observables with 'mutation status' as the predictive variable. Only genes mutated in >2 cell lines were included in the analysis, and a Benjamin-Hochberg multiple testing correction was used to identify significant results (FDR < 0.20). This quantitative assessment of pharmacogenomics uses an effect size parameter, calculated between wild type and mutant populations. If the effect size is >1, the difference in mean value between the mutated and wild-type populations is greater than the variance in at least one population, and the effect is therefore large.

Table 2. Mutated genes most significantly correlated to the activity of complexes **1** and **2**. The effect size measures the significance of this correlation between genomic status and cell susceptibility, the higher the effect size, the higher the correlation.

Complex	Mutated gene	No. cell lines	Effect size	FDR
1	*CASP8*	17	0.57	0.18
2	*KIT*	4	0.83	0.08

It is evident that when the *CASP8* gene is mutated, cells become sensitized to **1**. This gene encodes Caspase-8, which is involved in apoptosis and signalling cascades through TNF and NFkB. The only other drug in the screen for which *CASP8* coding mutation confers sensitivity is ABT-888 (veliparib), a PARP inhibitor. The PARP family of proteins are involved primarily in DNA repair and induction of programmed cell death. Where the DNA damage is beyond repair, PARP is inhibited so as to preserve cell ATP. The cell then undergoes programmed cell death.

The *KIT* gene coding mutation is associated with the sensitivity of four NSCLC cell lines to complex **2**, and encodes the human homolog of the proto-oncogene *C-KIT,* a type-III transmembrane receptor for the stem cell growth factor. Once bound to growth factor, this protein activates signal transduction through the cell, affecting cell survival and differentiation.

Matched pairs of patient-derived platinum sensitive and resistant ovarian cancer cell models

Matched pairs of ovarian cancer cells directly isolated from patients before and after relapse to platinum therapy are likely to better represent clinical drug resistance and relapse mechanism relative to drug resistant cell clones generated following *in vitro* drug exposure. Complexes **1** and **2** were tested in the matched patient-derived ovarian cancer cell lines PE01 (patient prior to treatment), PE04 (patient after taxane/platinum treatment)[22] and also PE01-CDDP (PE01 cells exposed to low levels of CDDP *in vitro* to create Pt resistance), Table 3.

Table 3. IC_{50} values for complexes **1** and **2** in patient-derived cancer cell lines. PE01 patient prior to treatment, PE04 patient after taxane/platinum treatment and PE01-CDDP cells from PE01 exposed to low levels of CDDP *in vitro* to create Pt resistance.

Complex	Cell line	IC_{50} (μM)
1	PE01	22.4
	PE04	64.3
	PE01-CDDP	110.3
2	PE01	1.21
	PE04	1.65
	PE01-CDDP	1.56

It can be seen from Table 3 that complex **2** maintains high activity in all 3 patient-derived cell lines. Conversely, **1** has poor activity in PE01 and loses activity in cells treated with taxane/CDDP and even more so in CDDP-resistant cells. This shows that the activity of **2** is unaffected by CDDP and/or taxane resistance in these ovarian cell lines, unlike **1**, suggesting a lack of cross resistance due to its different mechanism of action. Given the rise in occurrence of clinical platinum resistance, this is a promising finding for complex **2**.

Gene expression analysis

To investigate the MoA of the more active complex **2**, A2780 ovarian cancer cells were exposed to the IC_{50} concentration (0.40 μM) and the differential gene expression was explored using RNA sequencing across a 48 h time series; measuring gene expression after 4, 12, 24 and 48 h exposure.

Approximately 30 million 50 bp, paired-end reads were generated per sample, and sequence reads were mapped to the hg19 (GRCh37) human genome (ArrayExpress accession). Table S1 gives the sequencing statistics for the experiment.

Figure S3 shows multidimensional scaling (MDS) plots for complex **2**- and control-exposed samples across the time series. These plots are a means of visualising the level of similarity in sample sets, by placing each of them in *N*-dimensional space, where between-object distances are preserved.

The MDS plots show natural separation of the samples into clusters, and good agreement between the triplicate measurements. The biggest source of variation is by time point, followed by exposure-status, i.e. whether they are exposed to a control or to complex **2**. Figure S3B provides clear evidence that the samples exposed for 48 h are significantly different from those exposed for shorter time periods, both in the control and in the compound-exposed samples.

Figure S4A shows the number of differentially expressed genes (DEGs) at 4, 24 and 48 h, and highlights where differential expression overlapped. Figure S4B shows the number of those genes that were up- or down-regulated across the series. The highest number of differentially expressed genes was found after 12 h exposure (746) and 24 h (719), and significant differential expression (DE) after just 4 h exposure (349). Figure S4B shows that at 12 h, there is significantly more down-regulation than up-regulation, almost a 2:1 ratio, compared to 24 h, where there is ca. 1:1 ratio of up- and down-regulation.

We carried out pathway analysis with Ingenuity Pathway Analysis software which uses an extensive literature database (Ingenuity Knowledge Base) to integrate biological and chemical pathway perturbation information.[23] DEGs with $1.0 < \text{LogFC} > 1.0$ and $\text{FDR} < 0.05$ were assigned to biological pathways. Table S2 shows the top five upstream regulators of these pathways, across

the time series. The tables show the *p* value as calculated by a hypergeometric test of over representation, and the z-score that describes the extent of activation/inhibition of each pathway. One of the hurdles with using high-content assays is that a drug's MoA can be swamped by larger cellular responses, like cell survival/death and stress signalling which control often overlapping downstream processes. This makes it difficult to pinpoint the MoA, however, these results show that cells activate stress response pathways even after short times of exposure to organo-iridium complex **2**.

Since previous studies on complex **2** suggested that oxidative stress may be a part of its MoA, we examined the DE of oxidative stress response markers (Figure 4).[8] The NRF2 transcription factor (encoded by the *NFE2L2* gene) is involved in an important antioxidant response pathway, binding to the hARE (human antioxidant response element) cis-element to transactivate detoxifying/antioxidant genes. AP-1 complexes C-FOS/C-JUN and FRA-1/c-JUN, encoded by *FOS*, *FOSL1* and *JUN* genes, compete with NRF2 for binding to hARE to active antioxidant genes. Two domains of Nrf2 cooperatively bind CBP, a CREB binding protein, and synergistically activate transcription.[24]

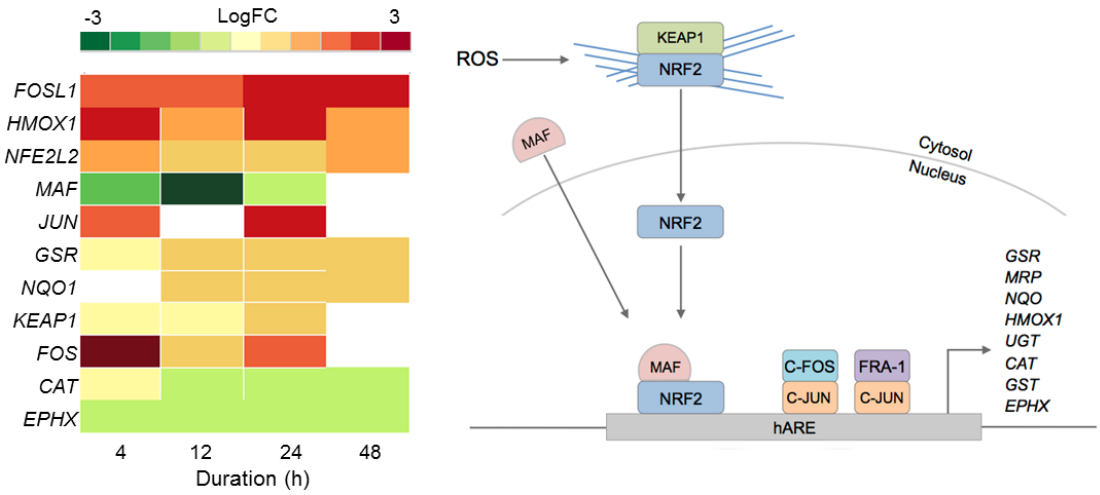

Fig. 4. Heat map of DEGs in the oxidative stress response pathway over the 48 h exposure of A2780 human ovarian cancer cells to complex **2**. Only DEGs with FDR < 0.10 are included.

Even though *NFE2L2* is up-regulated throughout the time series in response to **2**, the MAF co-factor is significantly down-regulated. Of the two AP-1 complexes, FRA-1 (*FOSL1*) is up-regulated throughout the time series, showing significant DE after just 4 h and highest expression after 24 h. The second AP-1 complex, with C-FOS (*FOS*) is also up-regulated for **2**, with the biggest response at 4 h, suggesting that the AP-1 complex may play a role during early exposure, and the FRA-1 complex a role in later exposure. Collectively this shows that all three transcription factors for oxidative stress response, NRF2 and the two AP-1 complexes, play a role in the cellular response to **2**.

Only a selection of antioxidant genes downstream of the transcriptional activators are up-regulated, and those that are up-regulated are not drastically so. Antioxidant genes *CAT* (catalase) and *EPHX* (epoxide hydrolase), are both down-regulated. *GSR* (glutathione reductase) and *NQO* (NADP(H) quinone oxidoreductase) are both up-regulated. The low-level expression of downstream effectors may suggest that A2780 ovarian cancer cells have a poor mechanism for responding to ROS.

Using flow cytometry, measurements were taken to assess the capability of **2** to generate ROS and superoxide (SO) in A2780 cells after 24 h exposure at IC_{50} concentration at 310 K (Figure S5). Table S3 highlights the results and shows a significant production of total ROS and SO in 84% of cells exposed to complex **2**, with the remaining 16% still showing significant levels of total ROS alone.

Given the similarity of iridium cyclopentadienyl complex **2** and osmium arene complex **3** (FY26) in the Sanger screen, the regulation of the ROS response pathway, as seen by RNA analysis, was also compared. In previous work, the same cell lines were exposed to FY26 at its IC_{50} concentration with the same protocol used here; DEGs were analysed across a 48 h time series (Figure S6).

Interestingly, although both compounds induce an oxidative stress response, there are differences in the components of the pathway that are up- and

down-regulated. For example, *FOS* is up-regulated in response to iridium complex **2**, but down-regulated in response to osmium FY26. This suggests that the oxidative stress response to complex **2** activates both AP-1 complexes, but activates only one in response to FY26.

Comparison of flow cytometry data for ROS measurements also supports a difference in the ROS levels in cells responding to **2** compared to FY26.[6] For example, when exposed to FY26, 95% of cells showed high total ROS and high SO levels, compared to the 84% in response to **2**. Yet, the levels of total ROS alone were drastically reduced in response to FY26, with only 2.5% of cells in this state, compared to 16% in response to **2**.

The apoptotic cell response in Figure S7 shows significant down-regulation of effector caspases after 12 h (*CASP-9, -6*, *-2, -3* and *-7)*. Genes for inhibitors of apoptosis proteins (IAP), which inhibit the activation of caspase proteins, such as *BIRC2* and more significantly *BIRC3*, are up-regulated after 4 h. *BIRC5*, which codes for survivin, another IAP, was down-regulated throughout the time series, suggesting specific modulation of apoptotic signals through caspase inhibition.

Protein microarrays

Zeptosens reverse phase protein microarrays (RPPA) were used to study the cellular levels of key proteins in **2**-exposed cells versus controls. RPPA measures the abundance of total protein levels and phosphorylated proteins using epitope-specific antibodies. The Relative Fluorescence Intensity (RFI) values obtained for each protein, following secondary fluorescent antibody detection, were normalized to a house-keeping protein in each sample (prohibitin) before the ratios of RFI between **2**-exposed and control samples were determined across the time-series (4, 24, 48 and 72 h), to quantify the abundance of total protein and phospho-epitopes relative to vehicle (DMSO) controls. Given the similarity in the Sanger screen between iridium complex **2** and the osmium complex **3** (FY26), we compared our previously published RPPA data to those of **2** to explore the DNA damage response.

During cellular response to DNA damage, ATM, among other proteins, is mobilised and auto-phosphorylated to ATM*, which in turn phosphorylates CHK2 to CHK2*. At this point, the response pathway branches into a rapid response via CDC25A, and a delayed response via p53 and p21. Figure 5 shows that the protein response reaches a peak at 24 and 72 h exposure, for both complex **2** and FY26.

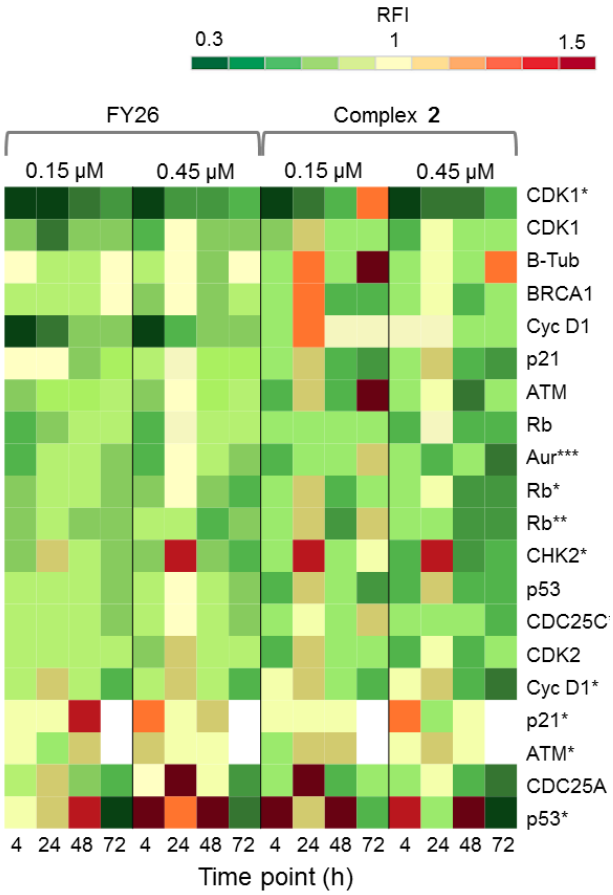

Fig. 5. DDR/Cell cycle investigations. Heat map showing the relative fluorescence intensity (RFI) values for a selection of DNA damage response (DDR) proteins in cells exposed to **2** across a 72 h time series. Data previously published for osmium complex FY26 are also included for comparison.[6] RFI values < 1 indicate a drug-induced decrease in protein levels, RFI = 1 indicates no-drug effect and RFI > 1 indicates drug-induced increases in protein levels.

CHK2*, CDC25A and p53* all show increased levels in response to both compounds. However, only **2** appears to mobilize a BRCA1 DNA damage response after 24 h, and primarily at a low concentration.

Additionally, after exposure to **2**, M-phase markers are detected, something not seen for FY26. For example, there is a high level of β-tubulin in response

to 0.15 μM **2** at both 24 and 72 h, with an additional increase in the levels of CDK1. This suggests that cells still have the proteins available to allow progression from G2 to M phase of the cell cycle. At the higher dose of **2**, both tubulin and CDK1 levels do not change from the control at 24 h. The higher levels of Rb* protein at 24 h suggest that cells have passed, or are at least able to pass, the G1/S transition point. This is not seen for FY26, for which levels of these proteins are lower in compound-exposed cells. Therefore, in response to **2**, cells may be held in late S phase, or G2 phase of the cell cycle, whereas in response to FY26 cells are more likely held in G1 phase.[25]

Flow cytometry experiments were performed on A2780 cells exposed to complex **2** and compared to those reported for FY26, to detect the populations of cells in various stages of the cell cycle (Figure 6). The red fluorescence of propidium iodide (PI) dye, which intercalates into DNA, correlates with the DNA content of the cells, and is twice as high in G2/M as in G0/G1 cells.

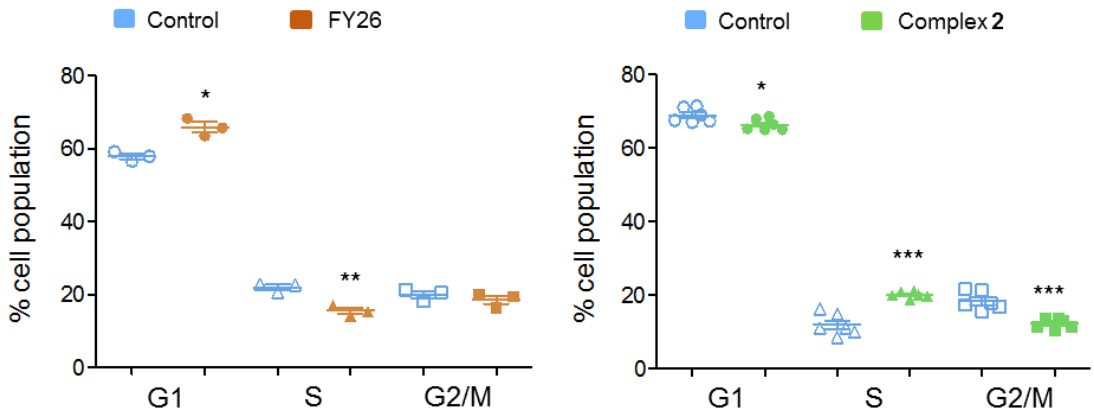

Fig. 6. Comparison of the effects of iridium complex **2** and osmium complex **3** on the population of the various phases of the A2780 cell cycle. Cell populations for control samples are shown in blue and those for 24 h **2**-exposed samples in green and **3**-exposed in brown. * indicates $p < 0.10$, ** indicates $p < 0.05$ and *** indicates $p < 0.01$ after a Welch two sample t-test between control- and compound-exposed samples in each stage of the cell cycle.

After 24 h exposure to **2**, the population of cells in the S phase of the cell cycle had increased, with subsequent G1 and G2/M populations decreasing. Conversely, exposure to **3 (**FY26) caused G1 arrest, with lower levels of cells populating the S-phase. S-phase arrest is often associated with compounds

that cause DNA damage, suggesting this could be a more prominent part of the MoA for complex **2**.

RPPA was also used to study further the differential levels of eighteen apoptotic proteins; five pro-survival proteins and thirteen pro-apoptotic proteins, in cells responding to **2** across a 72 h time series. This was compared to data previously reported for FY26 (complex **3**).

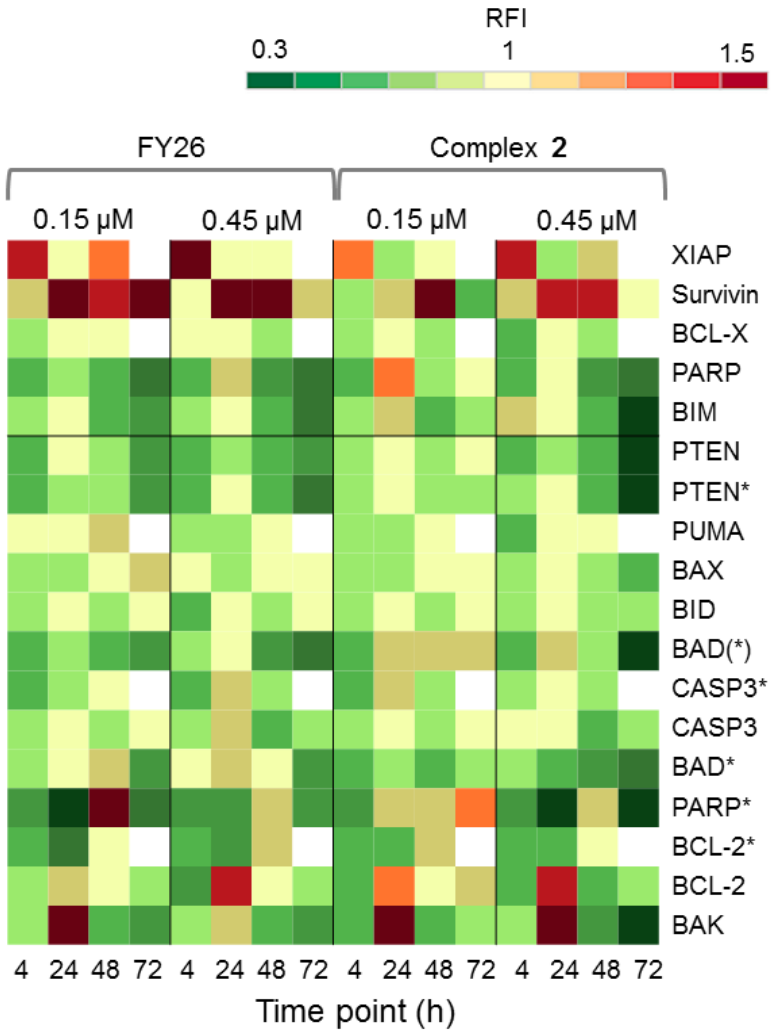

Fig. 7. Apoptosis investigations. Heat map showing the relative fluorescence intensity (RFI) values for a selection of apoptotic proteins in A2780 cells exposed to **2** across a 72 h time series. Data reported for **3** (FY26) are presented for comparison.[26]

Figure 7 shows that complex **2** induced high levels of IAP proteins, survivin and XIAP. Osmium complex **3** (FY26) also induced these same proteins, however, to a much lower level. BCL-X, which is a pro-survival protein located

in the mitochondria, was down-regulated during most of the time series, but up-regulated at 24 h, suggesting specific modulation of the apoptotic pathway. Of the pro-apoptotic proteins, most were down-regulated, however, BCL-2 and BAK, which are initiator proteins, were up-regulated at 24 h. In addition, PARP cleaved by CASP-3 (PARP*), was present in higher levels after 24 h, particularly at the lower concentration of administered compound.

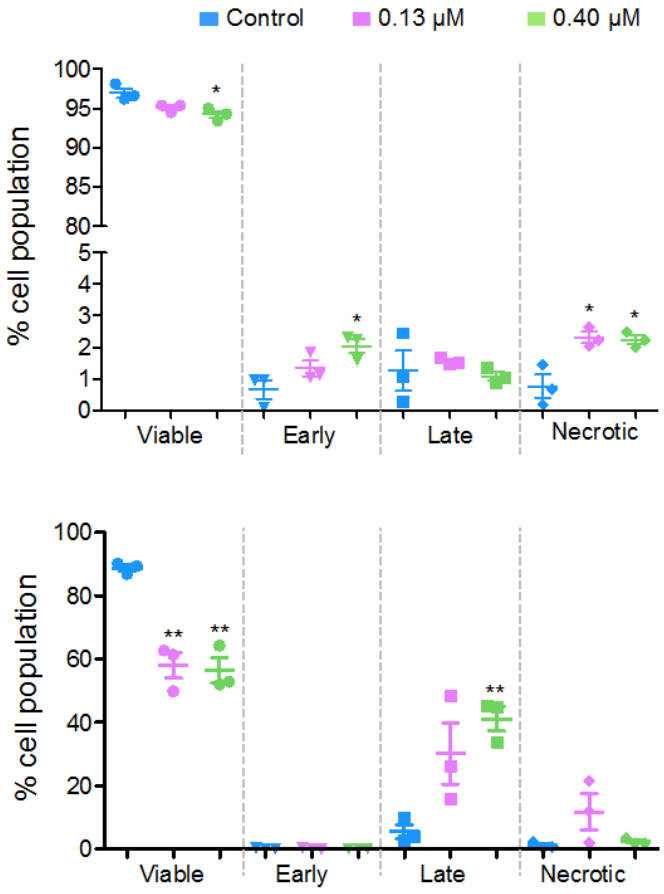

Fig. 8. The populations (%) of the various stages of apoptosis/cell death after exposure of A2780 human ovarian cancer cells to 0.13 µM (purple) or 0.40 µM (green) organo-iridium complex **2** for 24 h (top) and 48 h (bottom).

Flow cytometry studies were performed to determine the level of apoptotic cells after exposure to **2**. These experiments measure the fluorescence of annexin V and propidium iodide dyes, where the former identifies early apoptotic cells and the latter identifies late-apoptotic and/or necrotic cells. During early apoptosis, membrane-bound phosphatidylserine proteins, which ordinarily face into the cytoplasm, translocate to the outside of the cell

membrane and allow annexin V binding. A cell in early apoptosis, will still maintain its membrane integrity, therefore the DNA intercalator dye, propidium iodide, cannot pass through. Once the cell has lost viability, its membrane becomes permeable to propidium iodide, which fluoresces upon binding to DNA.

Figure 8 shows that there are different levels of apoptosis after 24 and 48 h exposure to **2**. After 24 h exposure, there was a slight decrease in cell viability, with a more significant decrease when exposed to a higher dose of **2** (94.2%) compared to the lower dose (95.1%). There was a higher population of cells in early apoptosis at the higher dose compared to the lower (2.0% and 1.3%, respectively), but a lower number of late apoptotic (1.1% and 1.5%) and necrotic cells (2.2% and 2.3%).

After 48 h there was a more significant drop in cell viability, now down to 58.0% at 0.13 μM and 56.4% at 0.40 μM complex **2**. There were on average, a larger population of cells in late apoptosis at the higher dose of **2** compared to the lower dose, 41.2% and 30.2%, respectively. However, there were more necrotic cells present after exposure to the lower dose of **2**, 11.8% and 2.5%.

Imaging

High content screening was used to further explore the mechanism of cell death in A2780 and OVCAR-3 ovarian cancer cells after 48 h exposure to various concentrations of **1** and **2**. After this period, adherent cells were stained with DAPI, a blue stain for nuclear DNA, and Nucview^{TM}488, a caspase 3 biosensor that becomes activated and fluorescent upon endogenous caspase activation inside the cell. Figure 9 shows representative microscopy images of caspase 3 positive apoptotic cells following exposure to 2.5 μM **1** and **2** for 48 h.

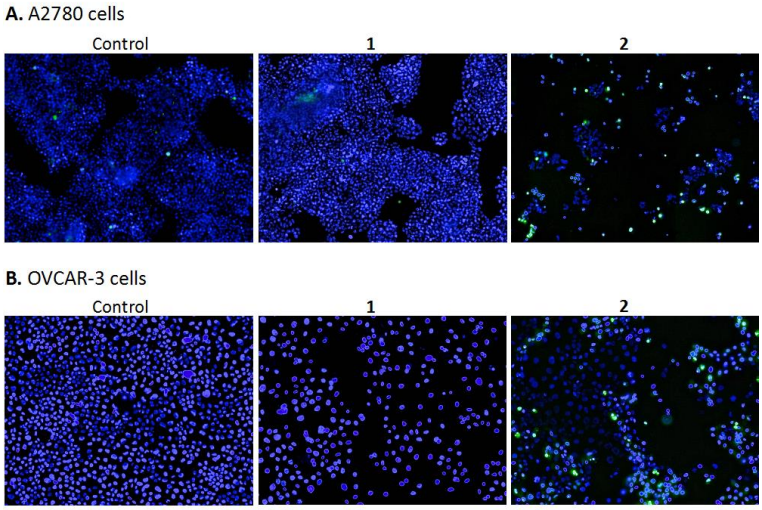

Fig. 9. Fluorescence images showing caspase positive apoptotic A2780 (A) and OVCAR-3 (B) human ovarian cancer cells 48 h after exposure to no added compound (control), 2.5 μM **1** and 2.5 μM **2**. DAPI stains nuclei of cells (blue), and NucView™ reagent stains caspase activity in apoptotic cells (green).

A2780 cells exposed to **1** and **2** show very different levels of apoptosis, with **1** inducing very little cell death compared to the DMSO control. Complex **2** shows significantly higher activity in both ovarian cell lines compared to **1,** particularly at the higher concentration of 2.5 μM (representative images in Figure 9). Comparing cell lines provided interesting results and highlights the difference in cell selectivity between **1** and **2**. In A2780 cells, **1** was inactive and **2** was highly active in reducing cell count, however, in OVCAR-3 cells the cell count reduction was more comparable (results not shown). In general, the activity of complexes at the single cell level[27] depends on the metal itself, its oxidation state, the types of metal and numbers of bound ligand atoms, and the coordination geometry.[28,29] Some complexes can be relatively inert and might reach the target site intact (as administered), but in general metal complexes are pro-drugs and may undergo metal- or ligand-based redox reactions as well as ligand substitution reactions before they reach targets.[30,31]

Discussion

Since we have adopted a phenotypic screening approach, attempting to optimise the design of complexes based on their chemical properties and their activity, the next stage after discovery of active complexes is to elucidate the nature of their MoA to guide further chemical optimization and/or patient selection strategies. In the present case our approach assessed correlations between anti-cancer activity and cell line gene mutations comparing patterns of activity with a range of previously screened compounds with known target sites. Comparing just the patterns of activity has already been fruitful on the smaller scale of the NCI-60 cell line screens.[8] In general, metallodrugs are likely to be multi-targeted, attack several biochemical pathways simultaneously, and require a systems pharmacology approach for analysis of activity.[32] We also compare these iridium complexes with two organo-osmium complexes for which we also have Sanger screening data. This comparison highlights the remarkable influence of the azopyridine ligand on activity.

In the present case, the major difference between complexes **1** and **2** is the change in the chelated ligand from a negatively-charged C,N-bound phenylpyridine (**1**) to a neutral N,N-bound N-dimethylphenylazopyridine (**2**). Hence the overall charge on the complex changes from 0 (neutral) to +1. However, we previously reported that replacing only one atom from the N,N-chelating ligand 2,2'-bipyridine in the Ir(III) pentamethylcyclopentadienyl complexes to a C,N-chelating ligand phenylpyridine leads to a significant increase in anticancer activity.[28,33] Therefore, the change in charge on the complex seems not to play a vital role in the control of their anticancer activity. In addition, we found that potency toward cancer cells increased with additional phenyl substitution on the Cp* ring: Cp^{xbiph} > Cp^{xph} > Cp^{*} for the cyclopentadienyl Ir(III) complexes.[10] Complex **1** also has an additional phenyl substituent on the cyclopentadienyl ring, which not only enhances lipophilicity but can also intercalate between DNA bases if that is an attack site. However, interestingly, the Cp^{xph} complex **2** displayed a more potent antiproliferative activity than the Cp^{xbiph} complex **1**. It seems that the azopyridine ligand plays a major role in the anticancer activity.[9] The azopyridine ligand is a strong π-acceptor, withdrawing electron density from the metal. This makes complex **2**

(as well as **3** and **4**) more inert towards hydrolysis than complex **1**, which more readily undergoes aquation (replacement of monodentate chloride with water) in aqueous media and leads to deactivation before reaching its biological targets.[30]

We have also shown previously for Os complexes **3** and **4**, that the additional phenyl group in **4** increases activity, but does not play a key role in the MOA. It is likely to increase cell uptake, resulting in a more potent compound.[34] This has also been shown for Ir complexes.[9]

Our previous work has shown the difference in activity between neutral complex **1** and a charged analogue, $[Ir(\eta^5\text{-}Cp^{xbiph})(ppy)py]^+$, in which the Cl ligand is substituted by pyridine. The charged complex has a higher potency, however, this was linked to the slower hydrolysis of the Ir-py bond, which affected the downstream MOA. However, in contrast, the Ir-Cl bond in complex **2** does not readily undergo hydrolysis**.** Thus even though previous work has demonstrated the importance in the Ir-Cl bond, the bidentate ligand seems to have a dominant effect, in line with the high activity of the Os-azopyridine complexes **3** and **4.**[34]

Pharmacogenomic screening

The antiproliferative potency of organo-iridium complexes **1** and **2** compared to CDDP towards the wide variety of cancer cell lines in both the NCI-60 and Sanger-ca. 900 cell lines follows the order: **2** > **1** > CDDP. Both the lipophilicity and overall charge on a complex can have a major effect on its biological activity. This trend is also apparent for patient-derived cancer cell lines which display distinct sensitivities to platinum agents (Table 2), where **1** has poor activity in all 3 cell lines, particularly in CDDP-resistant cell lines with IC_{50} values > 100 μM. Complex **2** and not **1** would therefore be a candidate for combating platinum resistant cancers and suggests that complex **2** might have a non-DNA-based mechanism of action, unlike CDDP.

The Sanger screen was used to identify cell lines of interest and to correlate activity with similarities in cell line genetics to explore the MoA. It is apparent

that **2** has a novel pattern of activity compared to other drugs in the Sanger screen for which data are available (Table 2). It is the only drug to have a sensitivity association with mutations in the *KIT* gene, primarily found in NSCLC. *KIT* encodes C-KIT, an important cytokine receptor commonly associated with blood and bone cancers. Once the receptor is activated it controls signalling for cell survival, proliferation and differentiation. *KIT* mutations have been associated with an increased sensitivity to imatinib and has been proposed as an important biomarker in imatinib treatment.[37] Functional C-KIT often confers chemoresistance by augmenting the expression of DNA repair genes. The mutated *KIT* gene may therefore render cells more sensitive to DNA damage, consistent with DNA attack being partly responsible for the activity of **2**, as discussed further below.[38]

Interestingly, the Sanger screen highlighted a significant similarity between **2** ([Ir(η^5-Cp^{xph})(azpy-NMe$_2$)Cl]$^+$) and two previously studied Os complexes: FY12 ([Os(η^6-bip)(azpy-NMe$_2$)I]$^+$) (**4**) and FY26 ([Os(η^6-*p*-cym)(azpy-NMe$_2$)I]$^+$), (**3**), Figure 1, suggesting that their activity is closely linked to the azpy-NMe$_2$ ligand, which is conserved across all three compounds. Moreover since Ir(III) and Os(II) are isoelectronic (outer shell electronic configuration 5d^6) and the complexes have similar 3D structures, global charges and probably log P values, it might be expected that they have similar profiles of biological activity. Although the activity of **2** does not correlate with that of any other drugs screened, those of organo-osmium complexes FY12 and FY26 do. Particularly noteworthy is the similarity in activity between FY26, bleomycin and SN-38 (the active metabolite of irinotecan, Camptosar), where cell lines with *R184* amplifications are more resistant to all three compounds. Bleomycin, used in the treatment of testicular, cervical, lymphoma and cancers of the head and neck, causes both single- and double-DNA strand breaks in cancer cells.[39] It can chelate iron, bind to DNA and react with oxygen to produce ROS, which damage DNA.

Topoisomerase enzymes are required for the unwinding of supercoiled DNA and the cutting and re-ligation of DNA during replication and protein synthesis. The active metabolite of irinotecan, SN-38, is a topoisomerase I (TOP1)

inhibitor.[40] TOP1 relaxes supercoiled DNA during replication and transcription, and generates and ligates cleaved single strands. Inhibitors of TOP1 prevent the ligation of cleaved strands, maintaining DNA breaks and activating cell death mechanisms in cancer cells.

Oxidative stress

The mitochondrion is the biggest source of ROS production in the cell, and mutations in OXPHOS machinery in A2780 cells perpetuate ROS production.[41] NRF2 is up-regulated in response to **2**, and we have shown by flow cytometry that this compound induces a significant ROS response. SO is normally converted to oxygen and H_2O_2 by superoxide dismutase (SOD), which is then broken down by catalase (CAT) to water and oxygen.[42] Neither *CAT* nor *SOD* genes were up-regulated after exposure to **2**. In fact, *CAT* was expressed in higher levels in the control samples, highlighting the oxidatively-stressed nature of A2780 cells, and that no response to H_2O_2 was mobilised after compound exposure. Disruption of CAT and SOD function has been shown to have a knock-on effect on the function of other antioxidant enzymes, potentiating the damage caused by ROS.[43] The down-regulation of key response genes suggests that **2** induces ROS production and also reduces the ability of A2780 cells to respond to excessive ROS.

The production of ROS from mitochondria has a cyclic effect on the function of mitochondria, potentiating the production of higher levels of ROS.[44] These ROS can damage mtDNA and proteins within the mitochondria, in addition to disrupting the polarisation of the mitochondrial membrane.[45] Mitocans, which target the bioenergetics of cancer cells and increase ROS, are becoming a focus of anticancer drug development.[46] ROS generation by **2** may also occur by other mechanisms, as well as through mitochondria, ROS production during cell stress is well documented, and occurs indirectly in response to many drugs, including CDDP.[47]

Complex **2** shared similarity in its stress response to the organo-osmium complex FY26, **3**. The Sanger screen points to close similarities in their MoAs. Previous experiments on FY26 have likewise demonstrated induction of ROS

in A2780 cells.[6] It seems clear that the azpy ligand plays a central role in inducing ROS by both these organo-iridium and organo-osmium complexes, however, the differences between the two structures causes a difference in ROS responses at the gene and the cellular level, with complex **2** resulting in high levels of total ROS but reduced levels of SO compared to FY26, and subsequently different transcriptional responses being activated.

Recently we have shown that although organo-osmium complex **3** is relatively inert in aqueous chemical solutions, it is activated in cancer cells and the iodide ligand is rapidly pumped out, and studies by nanofocussed x-ray fluorescence spectroscopy show that osmium from complex **3** localises in the mitochondria of human ovarian cancer cells.[48,49]

DNA damage and cell cycle arrest

Cells are equipped with mechanisms to repair DNA damage, however, ovarian cancers often lack the proper tools for DNA damage repair (DDR).[50] Resistance to conventional platinum therapy often originates from the ability of cancer cells to repair DNA lesions caused by CDDP, even in cell lines with DDR deficiencies.[51] DNA damage caused by CDDP is often not selective for cancer cells, and can be just as damaging to normal cells, especially with high-dose CDDP. In contrast, it is also possible to damage DNA through indirect mechanisms, and DNA is a well-known target for ROS, particularly guanine bases.[52] DNA damage caused indirectly by anticancer compounds, through selective ROS generation, could provide a more targeted approach to achieving this MoA.

There was measurable protein activation of DDR through the ATM-CHK2-p53-p21 pathway, however, there was also activation of the BRCA1 protein. RPPA suggested either S or G2/M phase arrest was possible in cells exposed to **2**, with S and G2/M phase protein markers up-regulated at 24 and at 72 h. Flow cytometry experiments confirmed S phase arrest after 24 h exposure (Figure 6). BRCA1 is an important protein in the S phase of the cell cycle during DNA damage and is required for homologous recombination and DNA damage-induced S and G2/M phase arrest.[53] It could therefore follow that **2**

does not require functional p53 for its MoA, as it does not require cells to be held in G1.

Collectively this could suggest that organo-iridium complex **2** has a more directed effect on DNA by exerting its activity either during DNA replication (S phase) or after the DNA content has been doubled (G2 phase). Organo-osmium complex FY26 appears to be most effective prior to DNA replication (G1 phase), and therefore may not have a DNA-focussed MoA.

Apoptosis

Modes of cell death can often be distinguished using whole cell imaging techniques.[54] However, specific protein and gene markers can also be studied. For example, apoptosis is normally characterised by caspase production, and by distinct budding of cell membrane structures into so-called apoptotic bodies. In contrast, oncosis involves swelling and not shrinking of the cell and is caused by non-specific cell injury.[55] Necrosis is commonly identified as its own mode of cell death, but in fact necrosis is the last stage in any cell death pathway, i.e. both oncosis and apoptosis lead to necrosis and cell death.

Most anti-cancer agents aim to activate apoptosis in cancer cells, simply because this is the most controlled form of cell death, involving phagocytosis in the final stages. However, cancer cells often develop mechanisms to evade apoptotic cell death which serves to highlight the merits of alternative mechanisms, like pyroptosis, an immune-induced mechanism of cell death.[56] RNAseq data suggested poor transcriptional activation of apoptotic caspase markers by **2**, but some transcription of apoptotic initiators. RPPA further supported this conclusion, with waves of apoptotic initiation towards the middle of the time course, followed by recovery towards the end (Figure 7). By comparison, FY26 showed even less up-regulation of apoptotic components.

Late apoptosis was detectable by flow cytometry for **2**-exposed cells at the 48 h time point. However, by 72 h, the cell population had recovered viability. This supports an occurrence of a wave of cell death. Using high content

screening (HCS) to detect levels of caspase-3, the effector-phase of apoptosis was explored. HCS proved to be a useful method in visualising cell death for multiple compounds; it was possible to extract compound- based trends and make predictions about the level of apoptosis at higher concentrations, where there was a significant increase in apoptotic cells at higher concentrations for **2** compared to **1**. ROS release has been shown to modulate apoptosis and may therefore play a central role in delaying apoptosis.[57]

Conclusions

Screening of two organo-iridium complexes in the Sanger screen of 916 cancer cell lines revealed a remarkably high potency for the phenylazopyridine complex **2** compared to the phenylpyridine organo-iridium complex **1** and the clinical platinum drug cisplatin (CDDP).

The screen also revealed a particularly high susceptibility of triple negative breast cell lines to **2**, and potential correlations to ROS-inducing drugs. Notably the pattern of activity of **2** towards the wide range of cancer cell lines was different to 253 previously screened drugs suggesting an unusual mechanism of action, but remarkably similar to organo-osmium complex FY26 which shares the same N,N-chelated phenylazopyridine ligand.

The MoA for both iridium complex **2** and osmium complex **3** appears to involve the rapid generation of ROS in cells, and can achieve selectivity for cancer versus normal cells since cancer cells have defective mitochondria, the usual source of ROS. However, more interesting is the difference in the exact nature of the ROS response triggered; with complex **2** inducing less of a superoxide response. This difference in the induction of ROS caused cells to arrest in S/G2 phase in response to **2**, whereas for **3** cells arrested in G1. Apoptosis seemed to be apparent after longer exposure periods, with interesting pro- and anti-apoptotic protein dynamics measured across the time series.

Ultimately this study provides a clear example of the benefits of combining different theoretical and experimental methods to explore novel and complex MoAs. In particular the combination of such methods can allow the separation of intricate differences in activity between compounds to interpret phenotypic response at molecular and cellular levels, which inform further preclinical development and clinical translation.

Materials and methods

Compound synthesis and characterisation

All compounds were synthesised and characterised as described previously.[8,21,33]

Antiproliferation assays

Complexes **1** and **2** were screened under the 'Genomics of Drug Sensitivity in Cancer' project at the Sanger Institute (Cambridge, UK).

Briefly, cells were seeded in 96 well plates at ca.15% confluency and left to incubate for 24 h at 310 K, 5% CO_2, 95% air and 100% relative humidity. Cells were treated with nine concentrations of each compound and returned to the incubator for 72 h. For suspension cell lines, cells were treated with compound immediately following plating, and returned to the incubator. Cells were stained and quantitation of fluorescent signal intensity was performed using a plate reader. IC_{50} values were returned to The University of Warwick for downstream analysis. MANOVA analysis was performed by the Sanger Bioinformatics Institute.

Primary cancer cell screening

Primary patient cell lines were seeded in 96 well plates with ca. 5000 cells per well in RPMI-1640 with 1% (v/v) 2 mM glutamine. The plates were incubated at 310 K for 48 h. Stock solutions of each compound were prepared and cells exposed across a dose range for a further 48 h. Cells were extracted and the MTT (3-(4,5-dimethylthiazol-2-yl)-2,5-diphenyltetrazolium bromide) assay (Life Technologies) was used to determine cell viability.

RNA sequencing

TruSeq kits (Illumina) were used to prepare samples for sequencing as per the manufacturer's guidelines. From total RNA, mRNA samples were purified, fragmented and reverse transcribed to cDNA. Sequencing libraries were produced, with incorporated barcodes to allow multiplexing. Samples were sequenced on an Illumina Hiseq2000 instrument across 5 lanes (6 samples

per lane). 50 base pair, paired-end reads were recorded producing ca. 60 million reads in total, per sample.

A2780 cells were seeded at 3 x 10^6 cells per 100 mm petri dish. Plates were incubated for 24 h at 310 K, 5% CO_2, 95% air and 100% relative humidity. Complex **2** (400 nM) and vehicle control solutions were added and after 4, 12, 24 and 48 h cells were collected and whole-cell RNA extracted (RNeasy plus mini kit, Qiagen). Samples were run on a NanoDrop 1000 spectrophotometer machine and the absorbance at 230, 260 and 280 nm recorded to calculate the 260/230 and 260/280 ratios. Samples with A260/230 >2.0 and A260/280 >1.9 were passed. The concentration of RNA in each solution was also estimated using the NanoDrop and was verified using a 2100 Agilent Bioanalyzer and an RNA 6000 Nano Kit (Agilent), and the Qubit assay (Life Technologies). All samples had a RNA integrity number (RIN) > 9.50. A minimum of 1 µg RNA for each sample was transferred to Oxford Genomics Centre (Wellcome Trust Centre for Human Genetics) in a total of 30 µL RNase free water in skirted 96 well plates.

Data deposition: The sequences reported in this paper have been deposited in ArrayExpress (accession E-MTAB-5991).

Data analysis

Preliminary filtering was performed on the data to remove all samples with quality scores (Q) < 20. FASTQ files for the forward and reverse reads were integrated and aligned to the hg19 (GRCh37) human genome using TopHat2. Files were returned to The University of Warwick in BAM format. Samtools (version 0.1.19-44428cd) was used to explore the raw BAM files, extracting chromosomal reads and summary statistics. BAM files were sorted by read name and then converted to SAM format. HTSeq (version 0.5.4p5) was used to map the read locations to genomic regions using the hg19 genome construct with the intersection-nonempty program option. Resulting mapped files, were then analysed for differential gene expression using the edgeR package (version 3.1.10) in the R statistical programme (version 3.0.2). A list of differentially expressed genes was obtained for each time point (4, 12, 24

and 48 h) and used together with Ingenuity Pathway Analysis software to assign significantly expressed genes to biological pathways.

Reverse phase protein microarrays (RPPA)

4 x 10^5 A2780 cells were seeded per well and cells were pre-incubated in drug-free media for 48 h. After this, cells were treated at 150 nM and 450 nM for 4, 24, 48 and 72 h. Control samples were treated with media containing 0.1% DMSO. Cell lysates were collected and deposited onto a Zeptosens chip. Chips were blocked and washed prior to performing a dual antibody immunoassay comprising of a 24 h incubation of primary antibodies followed by 2.5 h incubation with secondary Alexa-Fluor 647 conjugated antibody detection reagent. The immunostained arrays were imaged using the ZeptoREADER instrument and analysed using ZeptoView 3.1 software. Local normalisation of sample signal to a reference BSA grid was used to compensate for any intra- or inter-array/chip variation. RFI values were further normalised to a house keeping protein (Prohibitin) and to the negative control, to provide the final RFI to represent the relative abundance of total, phosphorylated and cleaved proteins in compound-treated samples relative to the DMSO control for each time point.

Apoptosis assays

A2780 cells were seeded at 1 x 10^6 cells per well in 6-well plates. Cells were preincubated in drug-free media at 310 K for 24 h in a 5% CO_2 humidified atmosphere. Drug/compound solutions were added and the cells left to incubate for a further 24, 48 or 72 h. Following exposure, the drug-containing medium was removed, and cells were washed, harvested and stained with Annexin V FITC and propidium iodide (Biovision, Annexin V-FITC Apoptosis Kit) according to the manufacturer's instructions. Control samples stained with just propidium iodide or Annexin V FITC were also included for compensation purposes. The samples were analysed using Beckton Dickinson FACScan with fluorescence detection running Cell Quest software (20000 events were collected from each sample). Data were processed using Flowjo software (version 7.2.5).

Cell cycle analysis

A2780 cells were seeded at a density of 1 x 10^6 cells per well in a 6-well plate and pre-incubated in drug-free media at 310 Kfor 24 h in a 5% CO_2 humidified atmosphere. Drug solutions were added and the cells left to incubate for a further 24 h. Cells were collected and washed twice with PBS. Cells were fixed with 70% ethanol and stored at -293 K for 24 h. For analysis, cells were transferred into PBS, incubated with RNase (0.2 mg/mL) and propidium iodide (0.05 mg/mL) for 40 min at 310 K and then analysed by flow cytometry using a Beckton Dickinson FACScan with fluorescence detection. The resulting DNA histograms were quantified using the FlowJo software (version 7.2.5).

High content screening (HCS)

Compounds **1** and **2** were imaged by HCS at The Edinburgh Cancer Research Centre. Cells were seeded in a 96-well plate at 5000 cells/well and incubated for 48 h before treatment with each compound for a further 48 h. Prior to image acquisition, cells were incubated with 4 μg/mL DAPI (Sigma D8417), and 1 μM NucView™ (Biotium) reagent for 0.5 h. Microscopic images of DAPI and NucView™ stained cells were acquired with a 10x objective and appropriate optical filters using the Olympus ScanR high-content imaging microscope. Merged images of DAPI and Nucview™ cells were created using the Olympus ScanR imaging software Cell-IR™.

Competing interests

We have no competing interests.

Author Contributions

JMH, IR.C, AFM, NOC, and PJS designed the research. JMH, IRC, AFM, BRR, ZL and NOC. performed the research. JMH, GMH, IRC, AFM, NOC., and PJS. analysed data; and JMH, GMH, IRC, NOC and PJS wrote the paper. All authors contributed to the final version.

Acknowledgements

We thank the European Research Council (grant 247450), the Wellcome Trust (grants 086357, 102696 and 107691) the Biotechnology and Biological Sciences Research Council (grant 324594, Systems Biology studentship for J.M.H.), Engineering and Physical Sciences Research Council (grant EP/F500378/1, MOAC Studentship for G.M.H.), Drs Ultan McDermott and Matthew Garnett (Sanger Institute) for their help and advice with the Sanger screening studies, and Professor David Wild (Warwick University) and EU COST Action CM1105 for helpful discussions.

References

1 D. Wang and S. J. Lippard, Cellular processing of platinum anticancer drugs, *Nat. Rev. Drug Deliv.*, 2005, **4**, 307–320.

2 P. M. Bruno, Y. Liu, G. Y. Park, J. Murai, C. E. Koch, T. J. Eisen, J. R. Pritchard, Y. Pommier, S. J. Lippard and M. T. Hemann, A subset of platinum-containing chemotherapeutic agents kills cells by inducing ribosome biogenesis stress, *Nat. Med.*, 2017, **23**, 1–13.

3 H. Kostrhunova, J. Florian, O. Novakova, A. F. A. Peacock, P. J. Sadler and V. Brabec, DNA interactions of monofunctional organometallic osmium(II) antitumor complexes in cell-free media, *J. Med. Chem.*, 2008, **51**, 3635–3643.

4 V. Novohradsky, Z. Liu, M. Vojtiskova, P. J. Sadler, V. Brabec and J. Kasparkova, Mechanism of cellular accumulation of an iridium(iii) pentamethylcyclopentadienyl anticancer complex containing a C,N-chelating ligand, *Metallomics*, 2014, **6**, 682–690.

5 C. G. J. and S. P. J. Fu Ying, Habtemariam Abraha, Basri M. B. H. Aida, Braddick Darren, Structure–activity relationships for organometallic osmium arene phenylazopyridine complexes with potent anticancer activity, *Dalt. Trans.*, 2011, **40**, 10553.

6 J. M. Hearn, I. Romero-Canelon, A. F. Munro, Y. Fu, A. M. Pizarro, M. J. Garnett, U. McDermott, N. O. Carragher and P. J. Sadler, Potent organo-osmium compound shifts metabolism in epithelial ovarian cancer cells., *Proc. Natl. Acad. Sci. U. S. A.*, 2015, **112**, E3800-5.

7 S. H. van Rijt, I. Romero-Canelón, Y. Fu, S. D. Shnyder and P. J. Sadler, Potent organometallic osmium compounds induce mitochondria-mediated apoptosis and S-phase cell cycle arrest in A549 non-small cell lung cancer cells., *Metallomics*, 2014, **6**, 1014–22.

8 J. M. Hearn, I. Romero-Canelón, B. Qamar, Z. Liu, I. Hands-Portman and P. J. Sadler, Organometallic iridium(III) anticancer complexes with

new mechanisms of action: NCI-60 screening, mitochondrial targeting, and apoptosis, *ACS Chem. Biol.*, 2013, **8**, 1335–1343.

9 Z. Liu, A. Habtemariam, A. M. Pizarro, S. A. Fletcher, A. Kisova, O. Vrana, L. Salassa, P. C. A. Bruijnincx, G. J. Clarkson, V. Brabec and P. J. Sadler, Organometallic half-sandwich iridium anticancer complexes, *J. Med. Chem.*, 2011, **54**, 3011–3026.

10 Z. Liu and P. J. Sadler, Organoiridium complexes: anticancer agents and catalysts., *Acc. Chem. Res.*, 2014, **47**, 1174–85.

11 K. D. Paull, R. H. Shoemaker, L. Hodes, A. Monks, D. A. Scudiero, L. Rubinstein, J. Plowman and M. R. Boyd, Display and analysis of patterns of differential activity of drugs against human tumor cell lines: Development of mean graph and COMPARE algorithm, *J. Natl. Cancer Inst.*, 1989, **81**, 1088–1092.

12 D. Sidler, A. Brockmann, J. Mueller, U. Nachbur, N. Corazza, P. Renzulli, A. Hemphill and T. Brunner, Thiazolide-induced apoptosis in colorectal cancer cells is mediated via the Jun kinase-Bim axis and reveals glutathione-S-transferase P1 as Achilles/' heel, *Oncogene*, 2012, **31**, 4095–4106.

13 Y.-P. Wang, L.-S. Zhou, Y.-Z. Zhao, S.-W. Wang, L.-L. Chen, L.-X. Liu, Z.-Q. Ling, F.-J. Hu, Y.-P. Sun, J.-Y. Zhang, C. Yang, Y. Yang, Y. Xiong, K.-L. Guan and D. Ye, Regulation of G6PD acetylation by SIRT2 and KAT9 modulates NADPH homeostasis and cell survival during oxidative stress, *EMBO J.*, 2014, **33**, 1304–1320.

14 J. E. Frank, Diagnosis and management of G6PD deficiency., *Am. Fam. Physician*, 2005, **72**, 1277–1282.

15 T. Efferth, U. Fabry, P. Glatte and R. Osieka, Increased induction of apoptosis in mononuclear cells of a glucose-6-phosphate dehydrogenase deficient patient, *J. Mol. Med.*, 1995, **73**, 47–49.

16 W. Yang, J. Soares, P. Greninger, E. J. Edelman, H. Lightfoot, S. Forbes, N. Bindal, D. Beare, J. A. Smith, I. R. Thompson, S. Ramaswamy, P. A. Futreal, D. A. Haber, M. R. Stratton, C. Benes, U. McDermott and M. J. Garnett, Genomics of Drug Sensitivity in Cancer (GDSC): A resource for therapeutic biomarker discovery in cancer cells, *Nucleic Acids Res.*, 2013, **41**, 955–961.

17 T. Sawada, Y. S. Chung, B. Nakata, T. Kubo, Y. Kondo, T. Sogabe, N. Onoda, Y. Ogawa, N. Yamada and M. Sowa, [Establishment and characterization of a human breast cancer cell line, OCUB-1]., *Hum. Cell*, 1994, **7**, 138–144.

18 T. Aas, A.-L. Børresen, S. Geisler, B. Smith-Sørensen, H. Johnsen, J. E. Varhaug, L. A. Akslen and P. E. Lønning, Specific P53 mutations are associated with de novo resistance to doxorubicin in breast cancer patients, *Nat. Med.*, 1996, **2**, 811–814.

19 Y. Wang, J. Chang, X. Liu, X. Zhang, S. Zhang, X. Zhang, D. Zhou and G. Zheng, Discovery of piperlongumine as a potential novel lead for the development of senolytic agents, *Aging (Albany. NY).*, 2016, **8**, 2915–2926.

20 L. Raj, T. Ide, A. U. Gurkar, M. Foley, M. Schenone, X. Li, N. J. Tolliday, T. R. Golub, S. A. Carr, A. F. Shamji, A. M. Stern, A. Mandinova, S. L. Schreiber and S. W. Lee, Selective killing of cancer cells with a small molecule targeting stress response to ROS, 2012, **475**, 231–234.

21 Y. Fu, A. Habtemariam, A. M. Pizarro, S. H. Van Rijt, D. J. Healey, P. A. Cooper, S. D. Shnyder, G. J. Clarkson and P. J. Sadler, Organometallic osmium arene complexes with potent cancer cell cytotoxicity, *J. Med. Chem.*, 2010, **53**, 8192–8196.
22 S. P. Langdon, S. S. Lawrie, F. G. Hay, M. M. Hawkes, a. McDonald, I. P. Hayward, D. J. Schol, J. Hilgers, R. C. F. Leonard and J. F. Smyth, Characterization and properties of nine human ovarian adenocarcinoma cell lines, *Cancer Res.*, 1988, **48**, 6166–6172.
23 Ingenuity Systems, Ingenuity Pathway Analysis.
24 Y. Katoh, K. Itoh, E. Yoshida, M. Miyagishi, A. Fukamizu and M. Yamamoto, Two domains of Nrf2 cooperatively bind CBP, a CREB binding protein, and synergistically activate transcription, *Genes to Cells*, 2001, **6**, 857–868.
25 I. Romero-Canelon, M. Mos and P. J. Sadler, Enhancement of Selectivity of an Organometallic Anticancer Agent by Redox Modulation, *J. Med. Chem.*, 2015, **58**, 7874–7880.
26 H. V Marquart, E. H. Olesen, A. A. Johnson, G. Damgaard and R. G. Leslie, A comparative study of normal B cells and the EBV-positive Burkitt's lymphoma cell line, Raji, as activators of the complement system, *Scand J Immunol*, 1997, **46**, 246–253.
27 P. Horvath, N. Aulner, M. Bickle, A. M. Davies, E. Del Nery, D. Ebner, M. C. Montoya, P. Ostling, V. Pietiainen, L. S. Price, S. L. Shorte, G. Turcatti, C. von Schantz and N. O. Carragher, Screening out irrelevant cell-based models of disease, *Nat Rev Drug Discov*, 2016, **15**, 751–769.
28 Z. Liu, L. Salassa, A. Habtemariam, A. M. Pizarro, G. J. Clarkson and P. J. Sadler, Contrasting reactivity and cancer cell cytotoxicity of isoelectronic organometallic iridium(III) complexes, *Inorg. Chem.*, 2011, **50**, 5777–5783.
29 N. P. E. Barry and P. J. Sadler, Exploration of the medical periodic table: towards new targets., *Chem. Commun. (Camb).*, 2013, **49**, 5106–31.
30 Z. Liu, I. Romero-Canelon, B. Qamar, J. M. Hearn, A. Habtemariam, N. P. E. Barry, A. M. Pizarro, G. J. Clarkson and P. J. Sadler, The potent oxidant anticancer activity of organoiridium catalysts, *Angew. Chemie - Int. Ed.*, 2014, **53**, 3941–3946.
31 C. Wang, J. Liu, Z. Tian, M. Tian, L. Tian, W. Zhao and Z. Liu, Half-Sandwich Iridium N-Heterocyclic Carbene Anticancer Complexes, *Dalt. Trans.*, 2017, 6870–6883.
32 J. Liu and M. Chen, Systems Pharmacology for the Study of Anticancer Drugs: Promises and Challenges, *Clin. Pharmacol. Biopharm.*, 2015, **4**, 140–142.
33 Z. Liu, A. Habtemariam, A. M. Pizarro, G. J. Clarkson and P. J. Sadler, Organometallic iridium(III) cyclopentadienyl anticancer complexes containing C,N-Chelating ligands, *Organometallics*, 2011, **30**, 4702–4710.
34 J. M. Hearn, I. Romero-Canelón, B. Qamar, Z. Liu, I. Hands-Portman and P. J. Sadler, Organometallic iridium (III) anticancer complexes with new mechanisms of action: NCI-60 screening, mitochondrial targeting, and apoptosis, *ACS Chem. Biol.*, 2013, **8**, 1335–1343.

35 Z. Liu, I. Romero-Canelõn, B. Qamar, J. M. Hearn, A. Habtemariam, N. P. E. Barry, A. M. Pizarro, G. J. Clarkson and P. J. Sadler, The potent oxidant anticancer activity of organoiridium catalysts, *Angew. Chemie - Int. Ed.*, 2014, **53**, 3941–3946.
36 J. H. Doroshow, A. Juhasz, Y. Ge, S. Holbeck, J. Lu, S. Antony, Y. Wu, G. Jiang and K. Roy, Antiproliferative mechanisms of action of the flavin dehydrogenase inhibitors diphenylene iodonium and di-2-thienyliodonium based on molecular profiling of the NCI-60 human tumor cell panel., *Biochem. Pharmacol.*, 2012, **83**, 1195–1207.
37 F. S. Hodi, C. L. Corless, A. Giobbie-Hurder, J. A. Fletcher, M. Zhu, A. Marino-Enriquez, P. Friedlander, R. Gonzalez, J. S. Weber, T. F. Gajewski, S. J. O'Day, K. B. Kim, D. Lawrence, K. T. Flaherty, J. J. Luke, F. A. Collichio, M. S. Ernstoff, M. C. Heinrich, C. Beadling, K. A. Zukotynski, J. T. Yap, A. D. Van Den Abbeele, G. D. Demetri and D. E. Fisher, Imatinib for melanomas harboring mutationally activated or amplified kit arising on mucosal, acral, and chronically sun-damaged skin, *J. Clin. Oncol.*, 2013, **31**, 3182–3190.
38 C. Wichmann, I. Quagliano-Lo Coco, Ö. Yildiz, L. Chen-Wichmann, H. Weber, T. Syzonenko, C. Döring, C. Brendel, K. Ponnusamy, A. Kinner, C. Brandts, R. Henschler and M. Grez, Activating c-KIT mutations confer oncogenic cooperativity and rescue RUNX1/ETO-induced DNA damage and apoptosis in human primary CD34+ hematopoietic progenitors, *Leukemia*, 2015, **29**, 279–289.
39 S. M. Hecht, Bleomycin : New Perspectives on the Mechanism of Action 1, 2000, 158–168.
40 R. Mullangi, P. Ahlawat and N. R. Srinivas, Irinotecan and its active metabolite, SN-38: Review of bioanalytical methods and recent update from clinical pharmacology perspectives, *Biomed. Chromatogr.*, 2010, **24**, 104–123.
41 S. I. Grivennikov and M. Karin, Inflammatory cytokines in cancer: tumour necrosis factor and interleukin 6 take the stage, *Ann. Rheum. Dis.*, 2011, **70**, i104–i108.
42 M. P. Murphy, How mitochondria produce reactive oxygen species, *Biochem. J.*, 2009, **417**, 1–13.
43 S. Turkseven, A. Kruger, C. J. Mingone, P. Kaminski, M. Inaba, L. F. Rodella, S. Ikehara, M. S. Wolin and N. G. Abraham, Antioxidant mechanism of heme oxygenase-1 involves an increase in superoxide dismutase and catalase in experimental diabetes., *Am. J. Physiol. Heart Circ. Physiol.*, 2005, **289**, H701–H707.
44 C. Henchcliffe and M. F. Beal, Mitochondrial biology and oxidative stress in Parkinson disease pathogenesis, *Nat Clin Pr. Neuro*, 2008, **4**, 600–609.
45 F. S. Hosnijeh, Q. Lan, N. Rothman, C. S. Liu, W. Cheng, A. Nieters, P. Guldberg, A. Tjønneland, D. Campa, A. Martino, H. Boeing, A. Trichopoulou, G. Masala, E. Weiderpass, M. Dorronsoro, J. Ram, B. Melin, A. S. Johansson, J. Malm, S. Borgquist, P. H. Peeters, H. B. Bueno-de-mesquita and N. Wareham, Mitochondrial DNA copy number and future risk of B-cell lymphoma in a nested case-control study in the prospective EPIC cohort, 2014, **124**, 530–535.
46 J. Neuzil, L. F. Dong, J. Rohlena, J. Truksa and S. J. Ralph,

Classification of mitocans, anti-cancer drugs acting on mitochondria, *Mitochondrion*, 2013, **13**, 199–208.
47 Y. Chen, P. Jungsuwadee, M. Vore, D. A. Butterfield and D. K. St. Clair, Collateral Damage in Cancer Chemotherapy: Oxidative Stress in Nontargeted Tissues, *Mol. Interv.*, 2007, **7**, 147–156.
48 C. Sanchez-Cano, I. Romero-Canelón, Y. Yang, I. J. Hands-Portman, S. Bohic, P. Cloetens and P. J. Sadler, Synchrotron X-Ray Fluorescence Nanoprobe Reveals Target Sites for Organo-Osmium Complex in Human Ovarian Cancer Cells, *Chem. - A Eur. J.*, 2017, 1–6.
49 R. J. Needham, C. Sanchez-Cano, X. Zhang, I. Romero-Canelón, A. Habtemariam, M. S. Cooper, L. Meszaros, G. J. Clarkson, P. J. Blower and P. J. Sadler, In-Cell Activation of Organo-Osmium(II) Anticancer Complexes, *Angew. Chemie Int. Ed.*, 2016, 1017–1020.
50 J. Assis, D. Pereira and R. Medeiros, Ovarian cancer and DNA repair: DNA ligase IV as a potential key., *World J. Clin. Oncol.*, 2013, **4**, 14–24.
51 L. Galluzzi, L. Senovilla, I. Vitale, J. Michels, I. Martins, O. Kepp, M. Castedo and G. Kroemer, Molecular mechanisms of cisplatin resistance, *Oncogene*, 2012, **31**, 1869–1883.
52 N. R. Jena, DNA damage by reactive species: Mechanisms, mutation and repair, *J. Biosci.*, 2012, **37**, 503–507.
53 N. Foray, D. Marot, A. Gabriel, V. Randrianarison, A. M. Carr, M. Perricaudet, A. Ashworth and P. Jeggo, A subset of ATM- and ATR-dependent phosphorylation events requires the BRCA1 protein, *EMBO J.*, 2003, **22**, 2860–2871.
54 G. Kroemer, L. Galluzzi, P. Vandenabeele, J. Abrams, E. Alnemri, E. Baehrecke, M. Blagosklonny, W. El-Deiry, P. Golstein, D. Green, M. Hengartner, R. Knight, S. Kumar, S. a Lipton, W. Malorni, G. Nuñez, M. Peter, J. Tschopp, J. Yuan, M. Piacentini, B. Zhivotovsky and G. Melino, Classification of Cell Death 2009, *Cell Death Differ.*, 2009, **16**, 3–11.
55 G. Majno and I. Joris, Apoptosis, oncosis, and necrosis. An overview of cell death., *Am. J. Pathol.*, 1995, **146**, 3–15.
56 T. Bergsbaken, S. L. Fink and B. T. Cookson, Pyroptosis: host cell death and inflammation, *Nat. Rev. Microbiol.*, 2010, **7**, 99–109.
57 H.-U. Simon, A. Haj-Yehia and F. Levi-Schaffer, Role of reactive oxygen species (ROS) in apoptosis induction, *Apoptosis*, 2000, **5**, 415–418.

Electronic Supplementary Information (ESI)

Pharmaco-genomic Investigations of Organo-iridium Anticancer Complexes Reveal Novel Mechanism of Action

Jessica M. Hearn, George M. Hughes, Isolda Romero-Canelón, Alison F. Munro, Belén Rubio-Ruiz, Zhe Liu, Neil O. Carragher, and Peter J. Sadler

Supplementary Material

Methods

Roswell Park Memorial Institute (RPMI-1640) medium, as well as foetal bovine serum, L-glutamine, penicillin/streptomycin mixture, trypsin, trypsin/EDTA, phosphate buffered saline (PBS) were purchased from PAA Laboratories GmbH. HPLC grade ethanol, β-mercaptoethanol, PI (>94%), Annexin V-FITC Apoptosis Detection Kit and RNAse A were obtained from Sigma Aldrich. For RNA sequencing, cell shredders and mini-prep kits were purchased from Qiagen.

Cell maintenance

The A2780, human ovarian carcinoma cell line was obtained from the European Collection of Cell Cultures (ECACC). Cells were grown in RPMI-1640 medium supplemented with 10% (v/v) foetal calf serum, 1% (v/v) 2 mM glutamine and 1% (v/v) penicillin (10 k units/mL)/streptomycin (10 mg/mL). All cells were maintained in 75 mL culture flasks at 310 K with 5% CO_2 humidified atmosphere. Cells were grown as adherent monolayers and split when 80-90% confluent, using 0.25% trypsin.

Screening in the Sanger cell panel

Briefly, cells were seeded in 96 well plates at ca.15% confluency and left to incubate for 24 h at 310 K, 5% CO_2, 95% air and 100% relative humidity. For adherent cell lines, cells were treated with nine concentrations of each compound (2-fold dilution series over 256-fold concentration range) and returned to the incubator for 72 h. Cells were then fixed with 4% formaldehyde for 30 min and stained with 1 μM Syto60 for 1 h. Quantitation of fluorescent signal intensity was performed using a plate reader at excitation/emission wavelengths of 630/695 nm. For suspension cell lines, cells were treated with compound immediately following plating, and returned to the incubator for 72 h. Cells were stained with 55 μg/mL Resazurin, prepared in glutathione-free medium, for 4 h. Quantitation of fluorescent signal intensity was performed using a plate reader at excitation/emission wavelengths of 535/595 nm. MANOVA analysis was performed by the Sanger Bioinformatics Institute. All Figures presented here were reconstructed using the R statistical programme.

RNA sequencing

Experimental

A2780 cells were seeded in P100 Petri dishes at 3 x 10^6 cells per plate in 10 mL RPMI-1640 medium. Plates were incubated for 24 h at 310 K, 5% CO_2, 95% air and 100% relative humidity. Stock solutions of each compound and of the vehicle control were prepared in 5% (v/v) DMSO, 10% (v/v) saline, and 85% (v/v) RPMI-1640 medium. Cells were exposed to complex **2** at a final concentration of 400 nM. The final DMSO concentration for all cell samples did not exceed 0.05% v/v. After compound addition, cells were incubated for a further 4, 12, 24 and 48 h. Medium was aspirated from cells and cells were washed twice with PBS before trypsinising and collection. To each sample, 600 µL RLT lysis buffer (Qiagen) was added and the samples vortexed. Lysate was pipetted directly into QIAshredder spin columns (Qiagen) and centrifuged. Lysate was transfered to gDNA eliminator spin columns (RNeasy plus mini kit, Qiagen) and centrifuged. Columns were discarded and 600 uL of 70% ethanol was added to each sample flow-through. Samples were transfered into RNeasy spin columns (RNeasy plus mini kit, Qiagen) and centrifuged. Column-bound RNA samples were washed with RW1 and RPE buffer (RNeasy plus mini kit, Qiagen) before RNA collection in 70 µL RNAse-free water. Samples were stored at 193 K for no more than 2 months. Samples were diluted 1:10 fold in RNAse-free water and run on a NanoDrop 1000 spectrophotometer machine and the absorbance at 230, 260 and 280 nm recorded to calculate the 260/230 and 260/280 ratios. Samples with A260/230 >2.0 and A260/280 >1.9 were passed. The concentration of RNA in each solution was also estimated using the NanoDrop and was verified using a 2100 Agilent Bioanalyzer and an RNA 6000 Nano Kit (Agilent), and the Qubit assay (Life Technologies). All samples had a RNA integrity number (RIN) > 9.50. A minimum of 1 µg RNA for each sample was transferred to Oxford Genomics Centre (Wellcome Trust Centre for Human Genetics) in a total of 30 µL RNAse-free water in skirted 96 well plates.

Reverse phase protein microarrays (RRPA)

4 x 10^5 A2780 cells were seeded per well in 6-well plates, with samples in duplicate. Cells were pre-incubated in drug-free media for 48 h at 310 K in a

5% CO_2 humidified atmosphere. After this, cells were treated at 150 nM and 450 nM of complex **2** for 4, 24, 48 and 72 h. Control samples were treated with medium containing 0.1% DMSO. Following exposure, drug-containing medium was removed, and cells were washed twice with PBS and lysed with CLB1 buffer (Zeptosens-Bayer) according to manufacturer's instructions. Cell lysates were normalised to a uniform protein concentration of 2 mg/mL with CLB1 buffer (Zeptosens-Bayer) prior to preparing a final 4-fold concentration series of; 0.2; 0.15; 0.1 and 0.75 mg/mL in spotting buffer CSBL1 (Zeptosens-Bayer). The diluted concentration series of each sample was printed onto hydrophobic Zeptosens protein microarray chips (ZeptoChip™, Zeptosens-Bayer) under environmentally controlled conditions (constant 50% humidity at 287 K) using a non-contact printer (Nanoplotter 2.1e, GeSiM). A single 400 pL droplet of each lysate concentration was deposited onto the Zeptosens chip. A reference grid of Alexa Fluor 647 conjugated BSA was spotted onto each sub-array, each sample concentration series was spotted in between reference columns. After array printing, the arrays were blocked with an aerosol of BSA solution using a custom designed nebuliser device (ZeptoFOG™, Zeptosen-Bayer) for 1.5 h to prevent non-specific antibody binding. The protein array chips were subsequently washed in double deionised water (DDW) and dried prior to performing a dual antibody immunoassay comprising of a 24 h incubation of primary antibodies followed by 2.5 h incubation with secondary Alexa Fluor 647 conjugated antibody detection reagent (anti-rabbit or anti-mouse 647 Fab, Invitrogen). Following secondary antibody incubation and a final wash step in BSA solution, the immunostained arrays were imaged using the ZeptoREADER instrument (Zeptosens-Bayer). For each-sub-array, five separate images were acquired using different exposure times ranging from 0.5-10 s. Microarray images representing the longest exposure without saturation of fluorescent signal detection were automatically selected for analysis using the ZeptoView™ 3.1 software. A weighted linear fit through the 4-fold concentration series was used to calculate the relative fluorescence intensity (RFI) value for each sample replicate. Local normalisation of sample signal to the reference BSA grid was used to compensate for any intra- or inter-array/chip variation. RFI values were further normalised to a house keeping protein and to the negative

control, to provide the final RFI to represent the relative abundance of total, phosphorylated and cleaved proteins in compound-treated samples relative to the DMSO control for each time point.

Table S1. Summary statistics for RNA sequencing experiment.

Sample number	Sample name	Total reads	% Mapped reads	Mean quality score
1	0 h control	58,453,334	98.53	36.5
2	0 h control	52,958,428	98.32	36.4
3	0 h control	52,411,032	98.11	36.5
4	0 h control	57,489,392	98.72	36.5
5	0 h control	53,112,138	97.75	36.5
6	0 h control	54,962,488	98.12	36.4
7	4 h control	82,071,522	98.19	34.4
8	4 h control	84,555,686	98.11	34.4
9	4 h control	73,333,434	97.93	34.4
10	4 h **3**	69,130,568	97.87	34.4
11	4 h **3**	59,742,704	97.99	34.5
12	4 h **3**	72,018,526	98.38	34.4
13	12 h control	50,690,134	97.87	36.4
14	12 h control	55,041,730	99.25	36.4
15	12 h control	60,723,390	97.88	36.4
16	12 h **3**	58,813,794	98.12	36.4
17	12 h **3**	57,945,078	98.82	36.4
18	12 h **3**	56,092,354	97.97	36.4
19	24 h control	60,331,926	98.14	35.6
20	24 h control	67,939,036	98.93	35.0
21	24 h control	59,240,982	98.09	35.6
22	24 h **3**	64,300,818	95.65	35.5
23	24 h **3**	61,522,272	98.48	35.6
24	24 h **3**	61,343,334	98.18	35.5

Table S2. Pathway analysis showing the top five most-mapped processes for DEGs with -1.0 < LogFC > 1.0 and FDR < 0.05 after exposure to **2**. IPA has identified pathways of interest, with associated significance *p*- and z-values.

Time point (h)	Upstream regulator	p-value	Activation z-score	Predicted activity
4	TNF	3.25×10^{-15}	3.676	Activated
	LY294002	2.67×10^{-14}	-2.413	Inhibited
	PDGF BB	2.15×10^{-13}	4.766	Activated
	TGFβ1	2.62×10^{-13}	3.063	Activated
	ERK	1.31×10^{-12}	4.221	Activated
12	TNF	1.48×10^{-14}	3.238	Activated
	UO126	2.19×10^{-11}	-2.470	Inhibited
	LY294002	2.34×10^{-11}	-2.466	Inhibited
	beta-estradiol	3.29×10^{-11}	-0.400	-
	TREM1	6.67×10^{-11}	1.771	Activated
24	TGFβ1	1.30×10^{-24}	2.206	Activated
	TNF	3.94×10^{-22}	6.101	Activated
	LPS	7.13×10^{-22}	7.223	Activated
	PDGF BB	1.33×10^{-21}	5.287	Activated
	beta-estradiol	3.42×10^{-21}	2.230	Activated
48	TNF	4.93×10^{-12}	3.646	Activated
	IL1β	7.74×10^{-09}	3.343	Activated
	LPS	1.87×10^{-09}	2.211	Activated
	ESR1	3.17×10^{-09}	0.282	-
	TGFβ1	3.48×10^{-09}	1.717	Activated

Table S3. Generation of total ROS and superoxide by complex **2** in A2780 ovarian carcinoma cells exposed to IC_{50} concentrations. Values obtained from triplicate experiments. Determination of statistical significance by two-sample independent Welch t-test assuming unequal variance: $p \leq 0.05$ *, $p \leq 0.01$ **, $p \leq 0.001$ ***, $p \leq 0.0001$ ****.

	High Superoxide	**High ROS and Superoxide**	**High ROS**	**Low ROS and Superoxide**
	FL1-FL2+	**FL1+FL2+**	**FL1+FL2-**	**FL1-FL2-**
	Q1	**Q2**	**Q3**	**Q4**
Neg CTL	0.17 ± 0.07	0	0	99.82 ± 0.07
Complex 2	0.1 ± 0.1	84 ± 1 ****	16 ± 1 ****	0.3 ± 0.5

Table S4. List of publicly-released compounds tested by the Sanger Institute in the cell line screen

681640
(5Z)-7-Oxozeaenol
17-AAG
A-443654
A-770041
ABT-263
ABT-869
ABT-888
AC220
AG-014699
AICAR
AKT inhibitor VIII
AMG-706
AP-24534
AR-42
AS601245
AS605240/KIN001-173
AT-7519
ATRA
AUY922
AV-951
AX11492
Axitinib
AZ628
AZD-0530
AZD-2281
AZD2281
AZD6244
AZD6244
AZD6482
AZD6482
AZD7762
AZD8055
BAY 61-3606
Bexarotene
BI-2536
BIBW2992
Bicalutamide
BIRB 0796
BIX02189
Bleomycin
BMN-673
BMS-345541
BMS-509744
BMS-536924
BMS-708163
BMS-754807
Bortezomib
Bosutinib
Bryostatin 1
BX-795
CAL-101
Camptothecin
CAY10603
CCT007093
CCT018159
CEP-701
Cetuximab
CGP-082996
CGP-60474
CH5424802
CHIR-99021
CHIR-99021
CI-1040
Cisplatin
CMK
CP466722
CP724714
CUDC-101
CX-5461
Cyclopamine
Cytarabine
Dasatinib
DMOG
Docetaxel
Doxorubicin
EHT 1864
EKB-569
Elesclomol
Embelin
Epothilone B
Erlotinib
Etoposide
EX-527
FH535
FK866
FR-180204
FTI-277
GDC-0449
GDC0941
GDC0941
Gefitinib
Gemcitabine
Genentech Cpd 10
GNF-2
GSK-1904529A
GSK-650394
GSK1070916
GSK1120212
GSK2118436
GSK2126458
GSK269962A
GSK429286A
GSK690693
GW 441756
GW843682X
HG-5-113-01
HG-5-88-01
HG-6-64-1 (KIN001-206)
I-BET
Imatinib
INCB-18424
IPA-3
JNJ-26854165
JNK Inhibitor VIII
JNK-9L
JQ1
JQ12
JW-7-24-1
JW-7-52-1
KIN001-055
KIN001-102
KIN001-135
KIN001-167/ZSTK474
KIN001-175/BX-912
KIN001-201/TAK-715
KIN001-236
KIN001-242/FMK
KIN001-244
KIN001-260
KIN001-266
KIN001-270
KU-55933
Lapatinib
LAQ824
Lenalidomide
LFM-A13
LY317615
Masitinib
Methotrexate
MG-132
Midostaurin
Mitomycin C
MK-2206
MLN4924
MP470
MPS-1-IN-1
MS-275
NG-25
Nilotinib
NPK76-II-72-1
NSC-207895
NSC-87877
NU-7441
Nutlin-3a

NVP-BEZ235
NVP-BHG712
NVP-TAE684
Obatoclax Mesylate
OSI-027
OSI-906
OSI-930
OSU-03012
PAC-1
Paclitaxel
Parthenolide
Pazopanib
PD-0325901
PD-0332991
PD-173074
PF-02341066
PF-4708671
PF-562271
PHA-665752
PHA-793887
PI-103
PIK-93
piperlongumine
PLX4720
PLX4720 (for rescreen control)
"PXD101, Belinostat"
Pyrimethamine
QL-VIII-58
QL-X-138
QL-XI-92
QL-XII-47
QL-XII-61
QS11
Rapamycin
RDEA119
RDEA119
RO-3306
Roscovitine
rTRAIL
S-Trityl-L-cysteine
Salubrinal
SB 216763
SB-505124
SB-715992
SB52334
SB590885
Shikonin
SL 0101-1
SN-38
SNX-2112
Sorafenib
STF-62247
Sunitinib
T0901317
Tamoxifen
Temozolomide
Temsirolimus
TG101348
TGX221
Thapsigargin
THZ-2-102-1
THZ-2-49
Tipifarnib
TL-1-85
TL-2-105
TPCA-1
Tubastatin A
TW 37
UNC0638
UNC0638
Vinblastine
Vinorelbine
VNLG/124
Vorinostat
VX-11e
VX-680
VX-702
WH-4-023
WZ-1-84
WZ3105
XAV 939
XL-184
XL-880
XMD11-85h
XMD13-2
XMD14-99
XMD15-27
XMD8-85
XMD8-92
Y-39983
YK 4-279
YM155
YM201636
Z-LLNle-CHO
ZG-10
"Zibotentan, ZD4054"
ZM-447439

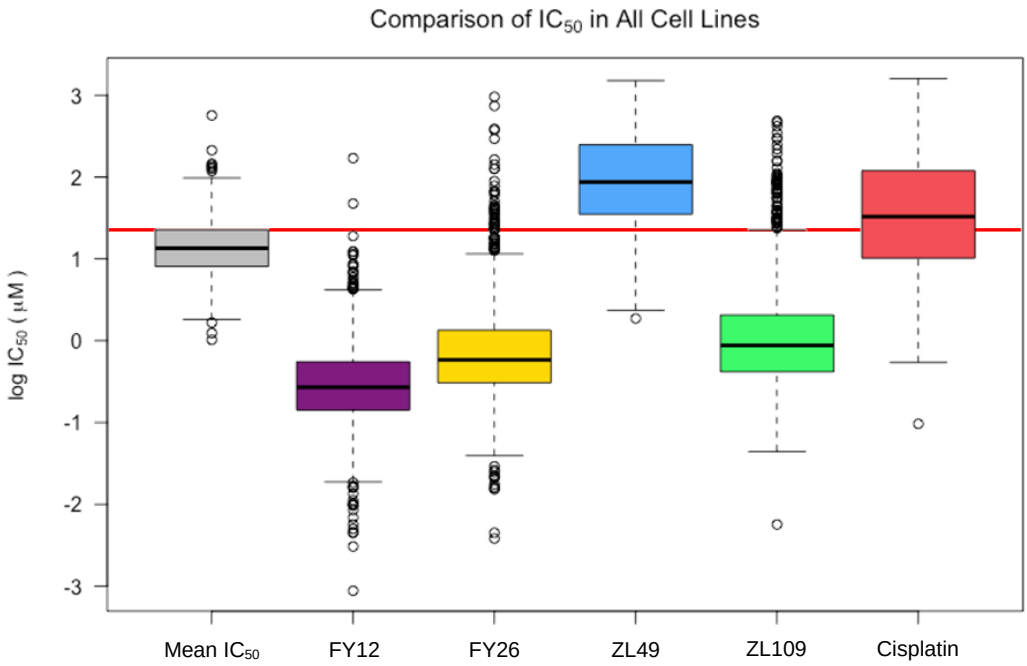

Figure S1. Box and whisker plot showing the distribution of log IC_{50} values for complexes **1** (ZL49) (blue), **2** (ZL109) (green) and CDDP (red) in all cell lines as well as the distribution of the mean log IC_{50} values for 202 drugs in the screen (grey). Cell lines which are less sensitive to **2** are highlighted in a red box. Data for osmium complexes **3** (FY26) and **4** (FY12) are also shown for comparison. For structures see Figure 1.

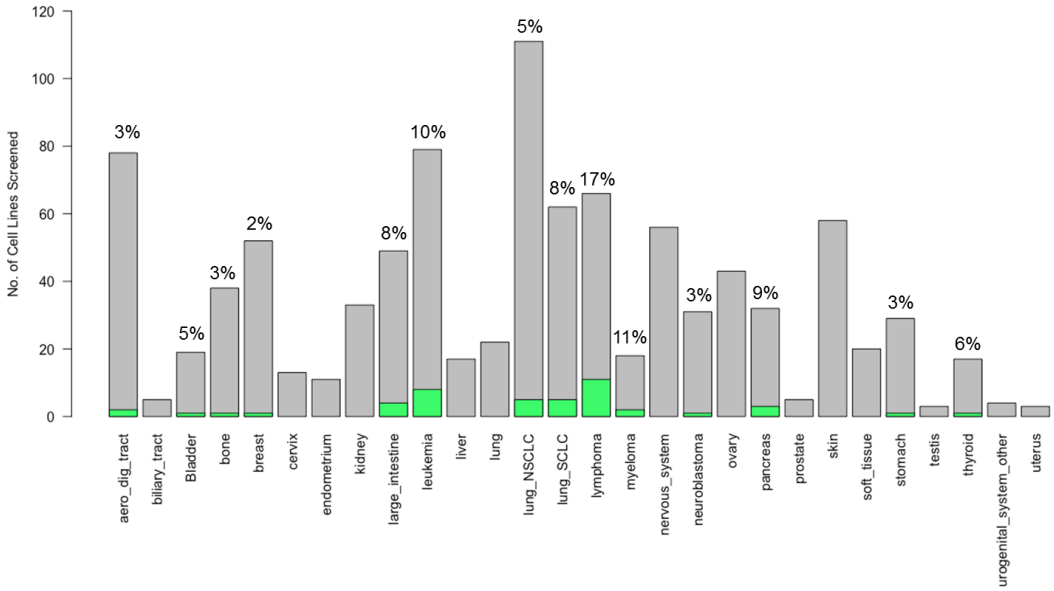

Figure S2. Bar plot of the number of cell lines in each tissue type screened against organo-iridium complex **2.** Cell lines significantly insensitive to **2** highlighted in green with the corresponding % of total cell lines of that type. Tissue groups where no percentage is given contained no cell lines resistant to **2**.

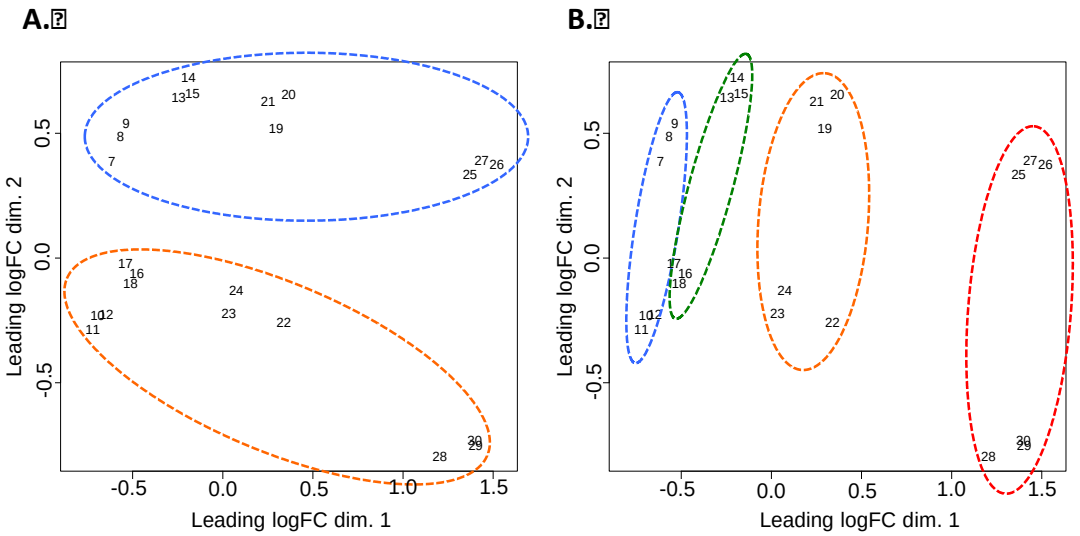

Figure S3. Multidimensional scaling (MDS) plots for RNA sequencing data. **(A)** Samples grouped as control (blue) and **2**-exposed (orange), demonstrating a differential drug-induced response. **(B)** Grouping of samples across the time series, with 4 h control and **2**-exposed samples in blue, 12 h in green, 24 h in orange and 48 h in red The contrasting behavior of the 48 h datasets compared to earlier time points is evident.

Figure S3 shows natural separation of the samples into clusters, and good agreement between the triplicate measurements. The biggest source of variation is by time point, the second by exposure-status, i.e. whether they are exposed as a control or to a compound.

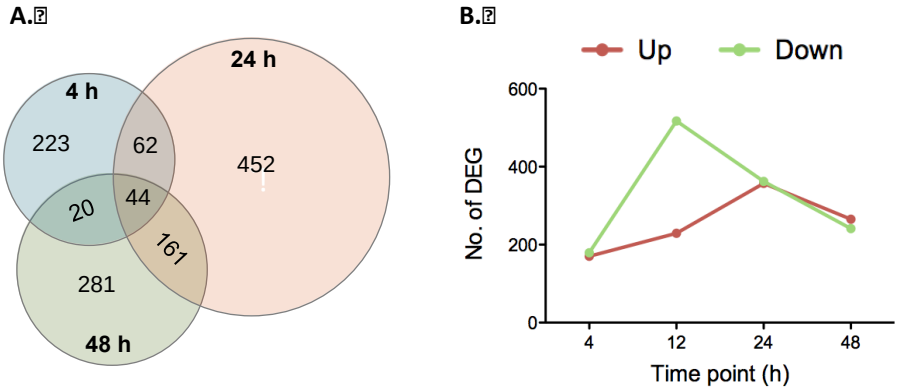

Figure S4. (A) Venn diagram showing the number of differentially-expressed genes at 4, 24 and 48 h after exposure to **2**. Only those genes with -1.0 < LogFC > 1.0 and FDR < 0.05 are included. **(B)** Graph showing the number of up- (red) and down-regulated (green) genes at each time point. Only those genes with -1.0 < LogFC > 1.0 and FDR < 0.05 are included.

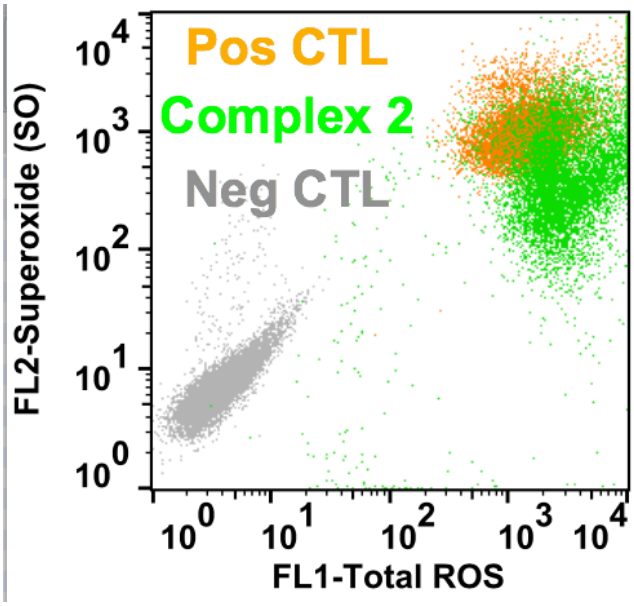

Figure S5. Generation of reactive oxygen species (ROS) and superoxide (SO) analysis by flow cytometry of A2780 ovarian carcinoma cells exposed to complex **2** for 24 h at IC_{50} concentration at 310 K. Cells stained with orange/green fluorescent reagents. Pyocyanin was the positive control (orange).

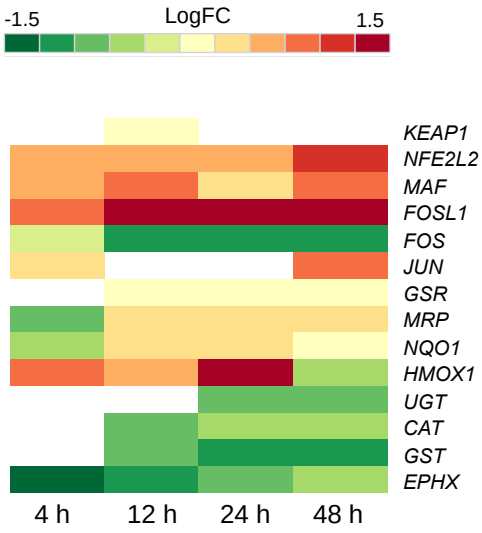

Figure S6. Heat map of DEGs In the oxidative stress response pathway in response to **FY26** (complex **3**) published previously.[1] Only DEGs with FDR < 0.10 are included.

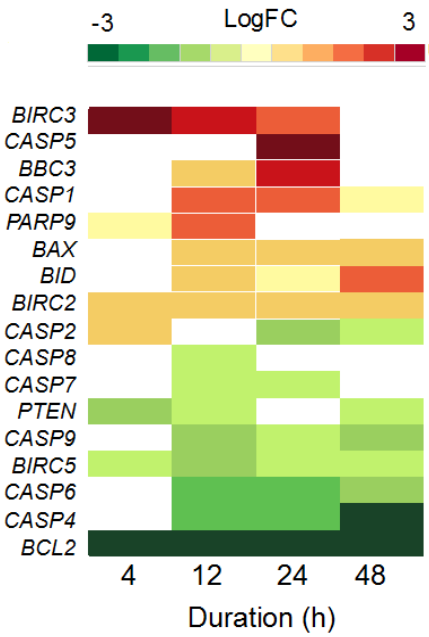

Figure S7. Heat map of DEGs for **ZL109** (complex **2**) in the apoptotic pathway. Only DEGs with FDR < 0.10 are included.

Reference

1 J. M. Hearn, I. Romero-Canelón, B. Qamar, Z. Liu, I. Hands-Portman and P. J. Sadler, Organometallic iridium(III) anticancer complexes with new mechanisms of action: NCI-60 screening, mitochondrial targeting, and apoptosis, *ACS Chem. Biol.*, 2013, **8**, 1335–1343.